1 **Novel roles of Kinesin-13 and Kinesin-8 during cell growth and division in the**

2 **moss *Physcomitrella patens***

3

4 Shu Yao Leong, Tomoya Edzuka, *Gohta Goshima, and *Moé Yamada

5

6 Division of Biological Science, Graduate School of Science, Nagoya University, Furo-cho,

7 Chikusa-ku, Nagoya 464-8602, Japan

8

9 *Corresponding authors: yamada.moe@a.mbox.nagoya-u.ac.jp; goshima@bio.nagoya-u.ac.jp

10

11

12 **Short title**: Kinesin-13 and Kinesin-8 in mitosis and tip-growth

13

14 **One sentence summary**: This study uncovered the roles of Kinesin-13 and Kinesin-8 in regulating

15 microtubule dynamics for mitotic spindle formation and straight tip cell growth in the moss

16 Physcomitrella patens

17

18

19 The authors responsible for distribution of materials integral to the findings presented in this article in

20 accordance with the policy described in the Instructions for Authors (www.plantcell.org) are: Moé

21 Yamada (yamada.moe@a.mbox.nagoya-u.ac.jp) and Gohta Goshima (goshima@bio.nagoya-u.ac.jp).

22

23

Abstract

24
25
26   Kinesin-13 and -8 are well-known microtubule (MT) depolymerases that regulate MT length and

27   chromosome movement in animal mitosis. While much is unknown about plant Kinesin-8, *Arabidopsis*

28   and rice Kinesin-13 have been shown to depolymerise MTs *in vitro*. However, mitotic function of both

29   kinesins has yet to be understood in plants. Here, we generated the complete null mutants in plants of

30   *Kinesin-13* and *-8* in the moss *Physcomitrella patens*. Both kinesins were found to be non-essential for

31   viability, but the *Kinesin-13* knockout (KO) line had increased mitotic duration and reduced spindle

32   length, whereas the *Kinesin-8* KO line did not display obvious mitotic defects. Surprisingly, spindle MT

33   poleward flux, for which Kinesin-13 is responsible for in animals, was retained in the absence of

34   Kinesin-13. Concurrently, MT depolymerase activity of either moss kinesins could not be observed,

35   with MT catastrophe inducing (Kinesin-13) or MT gliding (Kinesin-8) activity observed *in vitro*.

36   Interestingly, both KO lines showed waviness in their protonema filaments, which correlated with

37   positional instability of the MT foci in their tip cells. Taken together, the results suggest that plant

38   Kinesin-13 and -8 have diverged in both mitotic function and molecular activity, acquiring new roles in

39   regulating MT foci positioning for directed tip-growth.

40

41   **Key words**: *Physcomitrella patens*, mitosis, microtubule foci, microtubule dynamics, tip-growth,

42   Kinesin-13, Kinesin-8

43   **Running title**: Kinesin-13 and Kinesin-8 in mitosis and protonema tip-growth

44
45

Introduction

47

48   Microtubule (MT)-based motor proteins, Kinesins, form a large superfamily in animal and plant species

49   (61 genes in *Arabidopsis thaliana*, 78 in *Physcomitrella patens*, 45 in *Homo sapiens*, and 25 in

50   *Drosophila melanogaster*) (Reddy and Day, 2001; Miki et al., 2005; Shen et al., 2012). Kinesins show

51   various activities in association with MTs and play pivotal roles in eukaryotic cells, such as cargo

52   transport, MT organisation, MT dynamics regulation, and force generation (Walczak and Heald, 2008;

53   Hirokawa et al., 2009). Comprehensive functional analysis in several animal model systems, such as fly

54   and human cell lines, frog egg extracts, and mouse, together with biochemical characterisation of each

55   kinesin motor have provided insights into how MT-based intracellular processes are driven and

56   regulated during cell proliferation, differentiation, and animal development. In contrast, cellular and

57   developmental function of plant kinesins are less clear, partly due to the difficulty in making and

58   characterising the phenotypes of complete knockout (KO) lines of paralogous kinesins that likely

2

59 function redundantly. The use of high-resolution live microscopy, which was particularly critical for

60 assessing kinesin functions during mitosis in animals, has also been limited in plants.

61 Within the kinesin superfamily, Kinesin-13 and Kinesin-8 commonly show a unique activity *in*

62 *vitro*: MT depolymerisation (Desai et al., 1999; Howard and Hyman, 2007; Walczak et al., 2013). *In*

63 *vivo*, Kinesin-13 is able to depolymerise relatively stable MTs from both ends while MT catastrophe

64 inducing activity is limited to the plus-end (Rogers et al., 2004; Mennella et al., 2005). The best-studied

65 Kinesin-13, human KIF2C/MCAK, accumulates at MT ends either by diffusion or through recruitment

66 by other MAPs (Lee et al., 2008). At the ends, it binds to and stabilises protofilament bends, which

67 promotes strain on the association between protofilaments within the MT lattice (Moores et al., 2002;

68 Ovechkina et al., 2002; Ogawa et al., 2017). In the mitotic spindle, KIF2C/MCAK is localised to the

69 kinetochore and likely triggers depolymerisation of MT plus-ends that are erroneously attached to the

70 kinetochore (Kline-Smith et al., 2004; Walczak et al., 2013). Another Kinesin-13 (human KIF2A, fly

71 KLP10A) localises at the pole region and depolymerises MTs, including relatively stable kinetochore-

72 bound MTs, from the minus-end, driving poleward movement of MTs (called spindle MT poleward

73 flux) and chromosome segregation at anaphase (Rogers et al., 2004; Ganem et al., 2005; Walczak et al.,

74 2013). Depletion of Kinesin-13 causes various mitotic errors, such as spindle elongation, spindle

75 monopolarisation, erroneous kinetochore-MT attachment, and chromosome lagging at anaphase

76 (Walczak et al., 2013).

77 While Kinesin-13 does not show motility on MTs, Kinesin-8 possesses both MT depolymerising

78 activity and processive plus-end directed motility, and thus preferentially destabilises MT plus-ends

79 (Howard and Hyman, 2007; Walczak et al., 2013). During mitosis, Kinesin-8 concentrates at the outer

80 kinetochore region and prevents excessive elongation of kinetochore MTs and stabilises this

81 kinetochore-MT attachment to promote chromosome alignment to the spindle equator (Mayr et al.,

82 2007; Stumpff et al., 2008; Stumpff et al., 2012; Edzuka and Goshima, 2019). As a whole, Kinesin-13

83 and -8 MT depolymerisation activity is generally required for proper MT length regulation and correct

84 chromosome movement during mitosis of various animal cell types (Walczak et al., 2013). This mitotic

85 activity extends to cytokinesis, where Kinesin-13 and -8 also control anaphase spindle length and

86 bundling, respectively (Gatt et al., 2005; Uehara et al., 2013). Kinesin-13 and -8 are also repurposed for

87 interphase where mouse KIF2A (Kinesin-13) suppresses excessive axonal outgrowths (Homma et al.,

88 2003), and KIF24 (Kinesin-13) and KIF19 (Kinesin-8) have roles in regulating primary cilia formation

89 and cilia length, respectively (Kobayashi et al., 2011; Niwa et al., 2012).

90 Despite protein conservation, the function and activity of Kinesin-13 and -8 are not fully

91 understood in plants. Neither mutant phenotypes nor biochemical activity have been reported for

92 Kinesin-8. On the other hand, rice and *Arabidopsis* Kinesin-13s have been shown to preserve some

93 degree of MT depolymerisation activity *in vitro* and *in vivo* (Oda and Fukuda, 2013; Deng et al., 2015).

3

94   In *Arabidopsis thaliana* xylem vessel elements, Kinesin-13A is essential to create MT deficient areas in

95   the cortical MT network that is utilised as a scaffold for cellulose synthase movement. Cellulose is

96   deposited only at areas with patterned MTs, thus creating cellulose -lacking regions in MT deficient

97   areas, called pits, allowing for lateral transport of solutes and liquids in the plant. Knockdown of

98   Kinesin-13A by RNAi results in loss of MT patterning and smaller secondary cell wall pit formation

99   (Oda and Fukuda, 2013). Rice Kinesin-13A was shown to be important in regulating MT dynamicity

100   and organisation of the cortical MT network in a variety of cell types (Deng et al., 2015). However,

101   potency of the depolymerisation activity is uncertain, since plant Kinesin-13 lacks a domain required for

102   the robust activity of animal Kinesin-13 (Ovechkina et al., 2002; Lu et al., 2005) (Figure 1A comparing

103   animal and plant domains) and because overexpression of Kinesin-13A in non-xylem cells did not

104   depolymerise MTs unless coexpressed with an additional binding partner MIDD1 (Oda and Fukuda,

105   2013). On the other hand, Kinesin-13's function during mitosis is unknown as the *Kinesin-13A* mutants

106   in *Arabidopsis* and rice did not show mitotic defects. Moreover, *Arabidopsis* Kinesin-13s have been

107   suggested to be functionally redundant as complete null mutants were embryonic lethal (Fujikura et al.,

108   2014).

109   In the present study, the moss *Physcomitrella patens*, a model basal plant system, was used to

110   investigate Kinesin-13 and -8 function in general cellular processes, such as cell division. Using

111   homologous recombination and CRISPR gene editing techniques, all three paralogues of Kinesin-13

112   and -8 were knocked out, generating viable complete null mutants for each of the kinesin subfamilies.

113   We demonstrated that Kinesin-13 has a mitotic role in plants with *Kinesin-13* triple KO line having

114   longer prometaphase duration. However, spindle MT flux was still observed and shorter metaphase

115   spindles than the control were formed in the KO lines. In contrast, *Kinesin-8* triple KO line did not

116   display mitotic phenotypes. Unexpectedly, neither kinesin was shown to actively depolymerise MTs *in*

117   *vitro*; Kinesin-13 motor domain was able to induce MT catastrophe, while gliding activity of the

118   Kinesin-8 motor domain was confirmed. Notably, both KO lines had wavy protonema filaments, which

119   correlated with the MT foci abnormally fluctuating at the cell tip. Taken together, functional analyses of

120   *Kinesin-13* and *Kinesin-8* KO in moss revealed a divergence in mitotic function and molecular activity,

121   while revealing a novel role in regulating MT positioning for directed tip-growth.

122

123

Results

Kinesin-13 affects protonema growth, but not gametophore morphology

To investigate Kinesin-13's role in the moss *Physcomitrella patens,* all three paralogous *Kinesin-13* genes (*Kinesin-13a, -13b, -13c*) (Figure 1B) were sequentially deleted by homologous recombination mediated gene replacement in the moss lines expressing GFP-tubulin and histoneH2B-mRFP (Figure S1A, B). *Kinesin-13* single and double KO moss colonies did not have observable developmental defects. Moreover, *Kinesin-13* triple KO lines (hereafter *Kinesin-13* KO) were successfully generated, indicating that *Kinesin-13s* are not essential genes in moss. There was an overall reduction in colony size in the *Kinesin-13* KO when compared to the control (Figure 2A, 2B). However, the overall morphology of the protonema colonies, gametophore (leafy shoots encasing gametangia), and rhizoids (root-like filamentous cells differentiated from gametophore basal cells) (Cove, 2005; Menand et al., 2007; Kofuji and Hasebe, 2014) were indistinguishable from the control (Figure 2A, C), which differs from the case of rice *Kinesin-13A* mutant that shows small and round grains with shortened panicles and internodes of the whole rice plant (Kitagawa et al., 2010).

To further investigate the colony growth phenotype in the *Kinesin-13* KO moss, early stage moss colonies regenerated from single protoplasts cultured for 8 days were analysed for non-apical cell length and protonema filament branching pattern (Figure 2D–G). Non-apical cells, which undergo little cell expansion after cell division, were found to be shorter in the *Kinesin-13* KO moss caulonema cells (Figure 2E, F), consistent with reduced cell length in rice *Kinesin-13A* mutants (Deng et al., 2015). The branching pattern was analysed by measuring the parameters of branching distance (distances from tip of protonema filament to the first three branching sites), branch filament length, and branch angle (Figure 2E). While the first branching distance (distance from tip of protonema filament to nearest branching site) increased in the *Kinesin-13* KO line, other branching pattern parameters were not observably different from that of the control (Figure 2G).

Kinesin-13 facilitates spindle MT organisation and chromosome alignment, but does not drive spindle MT flux

The protonema tissue propagates by concerted asymmetric cell division and tip-growth in their apical stem cells (Rounds and Bezanilla, 2013). Therefore, a reduction in colony size in the *Kinesin-13* KO moss could be attributed to a defect in either or both events. To study mitosis in the *Kinesin-13* KO moss, localisation of moss Kinesin-13s to the mitotic spindle was first confirmed. As previously reported (Miki et al., 2014), moss Kinesin-13s showed spindle localisation, most enriched at the spindle equator, with the level of expression varying amongst the three paralogues; they did not show punctate signals at the spindle pole or kinetochore like animal Kinesin-13 (Supplemental Figure 2A). Next, time-

159 lapse imaging of moss protonema cells revealed that MT-dependent nuclear movement in prophase

160 was abnormal in the *Kinesin-13* KO line. In the control, nuclear movement is minimal or mildly

161 apically directed as cells undergo nuclear envelope breakdown (NEBD). In contrast, in the KO line, the

162 nucleus displayed severe retrograde movement leading up into NEBD and often continued moving

163 basally even during spindle establishment (Figure 3A, B). This retrograde nuclear movement was also

164 observed in the *Kinesin-13ac* double KO lines to a lesser degree, but not in the single or *Kinesin-13ab*

165 double KO lines (Figure 3B). Additionally, overexpression of Kinesin-13b(full-length)-Cerulean under

166 the *EF1α* promoter complemented the retrograde nuclear movement (Figure 3C, D). However, mutant

167 Kinesin-13b constructs in which motor activity (Kinesin-13b^{RIG}-Cerulean) (Dawson et al., 2007),

168 conserved MT depolymerisation motifs (Kinesin-13b$^{KVD/KEC}$-Cerulean) (Shipley et al., 2004), and a

169 conserved MT binding domain (Kinesin-13b^{Loop12}-Cerulean) (Soppina and Verhey, 2014) were

170 compromised could not restore the retrograde nuclear movement (Figure 3D). Overall, these results

171 suggest that Kinesin-13s contribute to nuclear movement redundantly in a motor-dependent manner.

172   The severe retrograde nuclear/spindle movement during prophase likely resulted in cross cell wall

173 positioning defects in the *Kinesin-13* KO moss. Indeed, analysis of subapical and apical cell length at

174 anaphase onset found that subapical cell length was reduced in the *Kinesin-13* KO moss (Figure 3E, F).

175 This correlates with reduction in non-apical cell length of early stage moss colonies, and suggests that

176 moss Kinesin-13 has a role in cell length maintenance.

177   Consistent with the retrograde nuclear/spindle movement, high-resolution time-lapse imaging

178 showed that *Kinesin-13* KO moss also has a disparity of the nucleus-surrounding MT array during

179 prophase (Figure 4A, Movie 1). In the control, shortly before NEBD, MTs associated asymmetrically to

180 the nucleus, with more MTs gathering on the apical side (Doonan et al., 1985; Nakaoka et al., 2012). In

181 contrast, this apically directed MT asymmetry was altered in the KO line, with the GFP-tubulin

182 intensity ratio of apical to basal hemispheres of the nucleus decreasing from ~1.2 in the control to ~1.0

183 (Figure 4B, C), suggesting that Kinesin-13s are important for MT organisation during prophase.

184   Upon NEBD, MTs assemble into a bipolar spindle. However, spindle assembly required more

185 time than control cells as anaphase onset was delayed, with the majority of the delay due to slow spindle

186 MT organisation as prometaphase was delayed but metaphase was unaffected (Figure 4D). Despite the

187 drastic nuclear movements and mitotic delay, MTs reorganised into the phragmoplast, which is the MT-

188 based machinery required for cell plate formation, and cytokinesis was completed in 15 out of 15 cells,

189 indicating that Kinesin-13s are dispensable in the later stages of cell division.

190   Unexpected from previous studies in animals and the predicted MT depolymerisation activity of

191 Kinesin-13, the metaphase spindle was shorter, rather than longer in the KO cells (Figure 4E). In animal

192 cells, MT depolymerisation at the spindle pole by Kinesin-13 is important for poleward flux of spindle

193 MTs, where tubulin is flowed from the spindle equator to the pole regions through the continuous

6

194   addition and removal of tubulin heterodimers at the plus- and minus-ends, respectively (Rogers et al.,

195   2005). To investigate if Kinesin-13 depletion affects poleward MT flux in moss, GFP-tubulin at the

196   equator of the mitotic spindle was bleached, and the movement of the photobleached strip was

197   monitored. Surprisingly, the strip migrated towards the poles as in control cells, indicating that MT

198   poleward flux took place in spite of complete Kinesin-13s depletion (Figure 4F, G, Movie 2). Thus,

199   Kinesin-13 contributes to mitosis in an unconventional manner in moss.

200

201   **Kinesin-13 regulates straight growth of the protonema filament by controlling the position of MT**

202   **focal points**

203   To study the colony growth defect of the *Kinesin-13* KO line in detail, long-term time-lapse imaging of

204   protonema filament growth was performed. Protonema filaments were found to be wavy with the

205   protonema cell tip periodically changing growth direction in the *Kinesin-13* KO line (Figure 5A, Movie

206   3). The *Kinesin-13* KO line was shown to be wavier with a bend frequency of 0.024 ± 0.002 μm^{-1}

207   (mean $\pm$ SEM; N = 26) compared to the control (0.006 ± 0.001 μm^{-1}, mean $\pm$ SEM; N =28) (Figure

208   5B). Interestingly, the *Kinesin-13ac* double KO line showed a milder wavy phenotype, while the single

209   and *Kinesin-13*ab double KO lines did not (Supplemental Figure 3A). Additionally, ectopic expression

210   of full-length Kinesin-13b rescued the waviness phenotype (Figure 5B, Supplemental Figure 3B). Thus,

211   Kinesin-13s are required for straight tip-growth.

212   Directionality of protonema tip-growth in moss has been stipulated to be dependent on MTs

213   (Doonan et al., 1988). At the apex of the protonema tip cell, plus-ends of MTs converge into a focus

214   known as the MT foci (Hiwatashi et al., 2014). This occupies about the same place as the focal point of

215   the actin filament cloud in a mutually dependent manner (Wu and Bezanilla, 2018; Yamada and

216   Goshima, 2018). Tip-growth defects including abnormal tip branching, retarded growth, and isotropic

217   growth are the phenotypes observed amongst transgenic mutants for regulators of cytoskeletal

218   dynamics where its organisation at the tip is impaired (actin related proteins, myo8, KINID kinesin,

219   KCH kinesin (Rounds and Bezanilla, 2013; Hiwatashi et al., 2014; Wu and Bezanilla, 2018; Yamada

220   and Goshima, 2018)). As such, it is possible that *Kinesin-13* depletion may result in defective MT

221   organisation at the cell tip, causing abnormal wavy protonema growth. MT foci behaviour in the

222   *Kinesin-13* KO line was investigated with spinning disc confocal microscopy where the MT foci of the

223   *Kinesin-13* KO moss was unstable and fluctuated frequently (Figure 5C, D, Movie 4). Interestingly, in

224   19 of 20 bending events observed, the displacement of the MT foci occurred prior to cell bending,

225   indicating that the MT foci dictated protonema growth direction (Supplemental Figure 4). These results

226   suggest that Kinesin-13s regulate anisotropic growth of protonema filaments by positional maintenance

227   of the MT foci at the cell tip.

228

Kinesin-13 is an interphase MT plus-end tracking protein

To investigate Kinesin-13's localisation during interphase, endogenously tagged Kinesin-13-Citrine lines (Miki et al., 2014) was observed with spinning disc confocal microscopy. Consistent with the depletion data, Kinesin-13s localised to the MT foci (Figure 6A and Supplemental Figure 2B). To address if Kinesin-13 also associates with individual MTs in the endoplasm, we utilised oblique illumination fluorescence microscopy that enables observation of single MTs near the cell cortex with reduced effect of chloroplast autofluorescence (Jonsson et al., 2015; Nakaoka et al., 2015). In the interphase MT array, Kinesin-13s accumulated at the ends of growing MTs and disappeared from ends when MTs switched to the shrink phase (Figure 6B, C, Supplemental Figure 2C, Movie 5). Since MT minus-ends are stabilised and exhibit little to no dynamicity in this cell type (Leong et al., 2018), we concluded that Kinesin-13 localises to the plus-ends of growing MTs. The plus-end tracking behaviour is reminiscent of human KIF2C/MCAK and *Drosophila* KLP10A, which are recruited by EB1 protein to growing plus-ends (Mennella et al., 2005; Lee et al., 2008).

MT shrink rate and rescue frequency increase while MT growth rate and catastrophe frequency reduce upon *Kinesin-13* depletion

Since Kinesin-13s tracked growing MT plus-ends, the effect of *Kinesin-13* deletion on MT plus-end dynamics during interphase was analysed using time-lapse oblique illumination imaging of GFP-tubulin. MT shrink rate increased upon *Kinesin-13* depletion, from 0.25 ± 0.01 μm/s (mean $\pm$ SEM; 5 MTs per cell analysed, N $=$ 25 cells) in the control to 0.43 ± 0.02 μm/s (mean $\pm$ SEM; 5 MTs per cell analysed, N $=$ 25 cells) in the KO line (Figure 6D). Catastrophe frequency reduced from 9.3 ± 1.2 x10^{-3}/s (mean $\pm$ SEM; N $=$ 33) in the control to 2.2 ± 0.5 x10^{-3}/s (mean $\pm$ SEM; N $=$ 28) in the KO line (Figure 6E), while rescue frequency increased from 14 ± 3 x10^{-3}/s (mean $\pm$ SEM; N $=$ 25) in the control to 25 ± 6 x10^{-3}/s (mean $\pm$ SEM; N $=$ 23) in the KO line (Figure 6F). To analyse MT growth rate, *Kinesin-13* KO moss expressing EB1-Citrine (Supplemental Figure 1C), a tracker of growing MT plus-ends, was imaged with oblique illumination fluorescence microscopy. MT growth rate based on EB1-Citrine comet movement reduced from 0.147 ± 0.013 μm/s (mean $\pm$ SEM; 10 MTs per cell analysed, N $=$ 5 cells) in the control to 0.093 ± 0.003 μm/s (mean $\pm$ SEM; 10 MTs per cell analysed, N $=$ 5 cells) in the KO lines (Figure 6G). The results suggest that Kinesin-13 plays a role in regulating MT dynamics in the interphase MT network.

Altered MT dynamics parameters may underlie MT length phenotypes in *Kinesin-13* KO

Depletion of MT depolymerases or catastrophe-promoting factors causes cytoplasmic MT lengthening and spindle expansion (Howard and Hyman, 2007; Goshima and Scholey, 2010). For example, in fission yeast cells lacking catastrophe-promoting factors, cytoplasmic MTs are more frequently

264   polymerised beyond the limits of the cell, resulting in MT bending and curling (West et al., 2001).

265   However, shorter metaphase spindle formation (Figure 4E) and the observation that the MT foci often is

266   unable to reach the apex of the cell tip in *Kinesin-13* KO lines (Supplemental Figure 5, Movie 4) appear

267   to be contradictory to this general rule. We reasoned that a decrease in MT growth rate and increase in

268   shrink rate might be limiting for overall MT length, despite significant reduction in catastrophe

269   frequency. To evaluate this idea, we built a probability model fixed by the parameters of MT growth

270   rate, shrink rate, catastrophe frequency, and rescue frequency, and ran a simulation in which 4,000 MTs

271   exhibit dynamic instability for 4 min (Figure 6H, Table 1). With control parameters, a normal

272   distribution was obtained where the 50% of MTs ranged from -12.4 to 23.4 µm lengths, and the longest

273   1000 MTs ranged between 23.4 to 59.8 µm lengths. In contrast, with MT dynamics parameters of

274   *Kinesin-13* KO cells, a narrower normal distribution was obtained, with 50% of MTs having lengths of

275   11.5 to 22.6 µm and the longest 1000 MTs ranged between 22.6 to 29.4 µm lengths. Thus, the

276   formation of shorter metaphase spindles and apex-displaced MT foci is a theoretically possible

277   outcome, and actually a more likely outcome, associated with depletion of moss *Kinesin-13* that affects

278   both MT catastrophe frequency and growth/shrink rate.

279

280   **Kinesin-13 motor domain induces catastrophe *in vitro***

281   To investigate the direct effect of moss Kinesin-13 on MT dynamics, recombinant Kinesin-13b^{motor}-

282   mGFP protein was expressed and purified from bacterial expression system (Figure 7A and

283   Supplemental Figure 5A; full-length Kinesin-13 could not be obtained in either bacteria or insect culture

284   cell expression system). The purified Kinesin-13b^{motor}-mGFP protein was subjected to 'binding-release'

285   experiments to confirm ATP hydrolysis activity: it bound to MTs in the presence of non-hydrolysable

286   ATP analogue (AMPPNP) and dissociated from MTs upon ATP addition (Supplemental Figure 5B).

287   The ATPase-active protein was added to GMPCPP-stabilised MTs, but did not show active MT

288   depolymerisation like that of animal Kinesin-13 protein (*Drosophila* KLP10A) (Figure 7B) (Rogers et

289   al., 2004; Moriwaki and Goshima, 2016). We considered the possibility of moss Kinesin-13 requiring a

290   binding partner like MIDD1 for *Arabidopsis* Kinesin-13 (Oda and Fukuda, 2013). BLAST search

291   showed that the moss does not have MIDD1 homologues, and so moss Kinesin-13 was tested for MT

292   depolymerisation activity in the presence of *Arabidopsis* MIDD1, but also did not depolymerise MTs

293   (Figure 7B). Overall, the purified Kinesin-13b^{motor}-mGFP construct did not exhibit MT depolymerase

294   activity under the current experimental condition..

295   The purified Kinesin-13b^{motor}-mGFP was also subjected to an *in vitro* MT polymerisation assay at

296   concentrations of 0, 0.15, 0.3, 0.6, 1.5 µM. While growth rate was somewhat reduced with higher

297   Kinesin-13b^{motor} concentration (Figure 7D), shrink rate and rescue frequency were not obviously

298   affected by Kinesin-13b^{motor}-mGFP addition (Figure 7E, F). Interestingly, in the presence of Kinesin-

9

299   13b^{motor}-mGFP, catastrophe frequency was reproducibly increased (Figure 7G). This result is consistent

300   with *in vivo* data in which MT catastrophe frequency decreased in the *Kinesin-13* KO line. In contrast,

301   the recombinant protein did not reproduce the plus-end accumulation seen *in vivo*, indicating that

302   truncated region and/or a separate factor may be required for plus-end recruitment.

303

Chromosome segregation and cell division proceed normally in the absence of Kinesin-8

305   Mitotic phenotype associated with Kinesin-13 deletion was fairly mild. We reasoned that another MT

306   depolymerase instead might have a major role in MT depolymerisation in mitosis of protonema

307   filaments, and thought to investigate Kinesin-8, which shows strong depolymerisation activity during

308   mitosis of yeast (Hildebrandt and Hoyt, 2000; Unsworth et al., 2008). To study Kinesin-8 function in

309   the moss, all three paralogous genes phylogenetically classed into the moss Kinesin-8 subfamily

310   (*Kinesin-8Ia, -8Ib, -8II*) (Shen et al., 2012; Miki et al., 2014) (Figure 1B) were knocked out

311   (Supplemental Figure 1D). Moss colonies, gametophores, and rhizoids were normal in the *Kinesin-8*

312   KO line (Figure 2A–C). High-resolution mitosis imaging did not show any defect in prophase MT

313   organisation, spindle formation, chromosome alignment, anaphase chromosome segregation, and

314   cytokinesis (9.1 ± 0.2 min from NEBD to anaphase onset; $N = 10$) (Figure 4A, D, E). We concluded

315   that Kinesin-8s are dispensable for mitotic cell division in moss protonema filaments.

316

Kinesin-8 controls positioning of the MT foci for straight tip growth

318   Interestingly, the *Kinesin-8* KO line also had wavy protonema filaments with bends occurring at smaller

319   magnitudes with a bend frequency of 0.022 ± 0.005 μm^{-1} (mean $\pm$ SEM; $N = 8$) (Figure 5A, B, Movie

320   3). Tracking of the MT foci at tip cells showed that it fluctuates more frequently in the *Kinesin-8* KO

321   line than in the control or *Kinesin-13* KO (Figure 5C, D, Movie 4), consistent with its smaller

322   magnitudes of bends.

323

Kinesin-8II^{motor} glides MT but does not show a MT depolymerisation activity *in vitro*

325   To analyse intrinsic activity of moss Kinesin-8, the recombinant Kinesin-8II^{motor}-GFP protein was

326   expressed and purified from bacterial expression system (Figure 8A, Supplemental Figure 5C) and was

327   subjected to a MT depolymerisation assay. 200 nM Kinesin-8II^{motor}-GFP was added to GMPCPP-

328   stabilised MTs but could not depolymerise them, while 200 nM *Saccharomyces cerevisiae* Kinesin-

329   8/Kip3 could depolymerise the MTs (Figure 8B). Kinesin-8II^{motor}-GFP was then tested for MT gliding

330   activity. Protein immobilised on silanised cover glass showed ability to glide GMPCPP-stabilised MTs

331   in an ATP-dependent manner, but also could not depolymerise those MTs (Figure 8C, D).

332

333

10

Discussion

334   **Discussion**

335

336   The KO lines generated in this study showed some characteristic phenotypes unreported in previous

337   plant kinesin mutants, such as wavy cell growth accompanying MT foci positional fluctuation (Kinesin-

338   13, Kinesin-8) and prophase MT disorganisation (Kinesin-13). Intriguingly, several processes driven by

339   these motors in many animal and yeast species were normal in their absence in moss, such as spindle

340   MT flux and chromosome segregation. Moreover, the hallmark activity of these kinesins, MT

341   depolymerisation, was not detected *in vitro*. Overall, this study provides a comprehensive view on the

342   roles of Kinesin-13 and -8 in a single plant species. Furthermore, our results reinforce the emerging

343   view that the kinesin superfamily is well conserved in plants but have diverged in their function

344   (Gicking et al., 2018; Nebenfuhr and Dixit, 2018).

345

346   **Are plant Kinesin-13 and -8 MT depolymerases?**

347   Kinesin-13 is a well-known MT depolymerase in animals. *Arabidopsis* and rice Kinesin-13s have also

348   been shown to depolymerise stabilised MTs (Oda and Fukuda, 2013; Deng et al., 2015). However,

349   moss Kinesin-13 only exhibited catastrophe-inducing activity *in vitro* and could not depolymerise

350   GMPCPP-stabilised MTs. This *in vitro* result is consistent with the reduced catastrophe frequency seen

351   with interphase MTs in the *Kinesin-13* KO moss. Nevertheless, 'negative' results obtained *in vitro* is not

352   necessarily conclusive: inappropriate expression systems or unsuitable biochemical environments could

353   prevent full activity of the protein. In this study, a motor-only construct was used due to technical

354   constraints. Thus, it is possible that other domain(s) on the *Kinesin-13* protein is required for MT

355   depolymerisation activity. One such element may be the coiled coil, which in animal *Kinesin-13*

356   dimerises the protein and increases MT depolymerisation activity (Hertzer et al., 2006). However, the

357   coiled coil region required for dimerisation is located immediately upstream/downstream of the motor

358   domain in animal Kinesin-13 (Maney et al., 2001), but is located further down the C-terminus in moss

359   Kinesin-13 (Figure 1A); it is unclear if dimerisation of moss Kinesin-13 could enhance the activity in a

360   similar manner to animal homologues. Furthermore, animal Kinesin-13 monomers are capable of

361   depolymerising MTs *in vitro* (Maney et al., 2001; Hertzer et al., 2006). It is also worth noting that moss

362   and also *Arabidopsis* Kinesin-13s lack the 'neck' domain that is important for strong MT

363   depolymerisation activity in animals (Ovechkina et al., 2002); based on this feature, it was indeed

364   originally speculated that plant Kinesin-13 might not have MT depolymerising activity (Lu et al., 2005).

365   Thus, although it is not ruled out that moss Kinesin-13 has a MT depolymerising activity, possibly with

366   the aid of a specific binding partner, it is enticing to say that it has diverged structurally and functionally

367   from animal Kinesin-13.

368   In cells, there is even less evidence to support Kinesin-13 as a MT depolymerase. Upon *Kinesin-13*

369   KO, interphase MTs show reduced MT growth rate and increased shrink rate. Such results instead point

370   to Kinesin-13 being a MT growth promoter. However, MT growth promoting activity was not

371   observed *in vitro*. This may be due to the use of the motor-only construct with which we could not

372   recapitulate the plus-end enrichment of Kinesin-13. Alternatively, considering the decrease and increase

373   in catastrophe and rescue frequency of interphase MTs, it is possible the Kinesin-13 regulates growth

374   and shrink rate indirectly via tubulin cycling: reduced catastrophe would result in reduced availability of

375   tubulin in the free tubulin pool, which might affect MT growth and shrink rates, as was proposed in the

376   studies of *Arabidopsis* ARK proteins (Eng and Wasteneys, 2014) and more recently with plant-specific

377   MT nucleator MACET4 (Schmidt and Smertenko, 2019).

378   Similar to Kinesin-13, we could not observe MT depolymerisation of the Kinesin-8 motor in our

379   assay, which differs from human and yeast Kinesin-8. This might be due to our use of truncated

380   construct (~440 a.a.) as we failed to purify the longer construct (~640 a.a.). However, we recently found

381   that *Drosophila* Kinesin-8 (full-length) shows plus-end directed motility and induces MT catastrophe at

382   the plus end, but is not able to depolymerise stable MTs *in vitro* (Edzuka and Goshima, 2019). Similar

383   activities might be endowed to moss Kinesin-8.

384

385   **Kinesin-13 and -8 for mitosis**

386   We could not detect any phenotypes in *Kinesin-8* KO lines during mitotic cell division, such as

387   chromosome alignment and mitotic delay, which are common phenotypes observed in yeast and animal

388   cells, suggesting that Kinesin-8 has lost mitotic functions in moss. In contrast, some but not all known

389   mitotic functions of Kinesin-13 (Walczak et al., 2013) were observed in moss. In animal mitosis,

390   centrosomal MTs (astral MTs) are overly developed during prophase in the absence of Kinesin-13

391   (Goshima and Vale, 2003; Rogers et al., 2004). Similarly, disorganised MTs were observed around the

392   nucleus, despite the loss of centrosomes in moss (and all other land plants). Nucleus surrounding MTs

393   may act as MTOCs equivalent to animal centrosomes. During prometaphase, kinetochore-MT

394   attachment appears to be less efficient, since prometaphase duration was slightly prolonged; whether

395   this was due to overall MT dynamics change or the lack of error correction, like the case of

396   KIF2C/MCAK depletion in animal cells, remains elusive. Spindle monopolarisation that was observed

397   in centrosome-containing animal cells (Goshima and Vale, 2003) was not detected. At metaphase,

398   Kinesin-13 in animal cells acts as a MT depolymerase at the pole, driving MT poleward flux and

399   halting spindle extension. Surprisingly, we could not obtain data that moss Kinesin-13 plays such a role:

400   Kinesin-13 does not localised at the spindle pole, MT flux was detected in the *Kinesin-13* KO line, and

401   the spindle was shorter, rather than longer, in the complete absence of Kinesin-13. MT dynamics is a

402   major contributor to spindle length regulation in animal somatic cells (Goshima and Scholey, 2010);

403   therefore, shortening might be due to the reduced MT growth rate observed in the endoplasm,

404   consistent with Kinesin-13 localising at spindle equator where MT plus-ends are enriched.

405   Chromosome segregation during anaphase A was normal, further supporting the notion that Kinesin-13

406   does not act as a MT depolymerase at the pole. These data indicate that the moss mitotic spindle

407   possesses a mechanism to drive spindle MT poleward flux independent of Kinesin-13.

408

409   Kinesin-13 and -8 for tip growth

410   The most prominent phenotype observed both in the *Kinesin-13* and *-8* KO lines was the tip-growth

411   defect. Recent studies suggest the importance of the MT converging centre, the MT foci, in protonema

412   tip-growth in moss, where F-actin, which is absolutely essential for tip-growth, is concentrated near the

413   MT foci. In several mutants of MT-associated motors in which tip grows more slowly, the MT foci is

414   not persistently formed (Hiwatashi et al., 2014; Wu and Bezanilla, 2018; Yamada and Goshima, 2018).

415   These transient MT foci produced bursts of MT concentration at random locations along the tip region

416   of the apical cell, causing the bending of the protonema filament at abrupt angles (Hiwatashi et al.,

417   2014). Such phenotypes are similar to tip-growth defects seen when moss is treated with MT disruptive

418   drugs (Doonan et al., 1988). Different from those mutants, we persistently observed a single MT focus

419   in the *Kinesin-13* or *-8* KO. However, their positions were unstable, exhibiting the waviness of rather

420   regular amplitude and frequencies. This suggests that Kinesin-13 and -8 play a role in MT foci

421   positional guidance, rather than MT foci formation/maintenance, which ensures straight growth of the

422   protonema filament. While straight tip-growth with limited MT foci fluctuations would allow fastest

423   propagation of moss, wavy growth would be an advantageous mechanism to facilitate innovative

424   exploration of the environment. Our study highlights the regulation of MT plus-end dynamics by MAPs

425   as an intracellular mechanism to modulate cell growth in response to environmental cues, reminiscent

426   of axon guidance in neurons (Sabry et al., 1991; Tanaka et al., 1995; Menon and Gupton, 2016).

427

428   Materials & Methods

429

430   Molecular cloning and gene targeting experiments

431   All transgenic moss lines, plasmids, and primers used in this study are listed in Table S1, S2 and S3

432   respectively; all lines originated from the *Physcomitrella patens* Gransden 2004 strain. Moss culture,

433   transformation, and transgenic line selection were performed as previously described (Yamada et al.,

434   2016). In brief, moss cells were cultured on BCDAT or BCD media under 24 h light illumination, and

435   transformation was performed by the standard PEG-mediated method.

436

13

437 _KO moss generation_ Kinesin-13 KO (GPH0438) and _Kinesin-8_ KO (GPH0433) were generated in the

438 moss strain expressing GFP-tubulin and histone-H2B-mRFP (Nakaoka et al., 2012) sequentially

439 replacing the targeted genes with antibiotic resistance using homologous recombination (HR). To do

440 this, 1 kb of genomic DNA sequences upstream/downstream of start/stop codons of the target genes

441 were cloned around an antibiotic resistance cassette, and then transformed into the moss. To knock out

442 _Kinesin-13_ genes in the moss expressing EB1-Citrine and mCherry-tubulin (Kosetsu et al., 2013),

443 _Kinesin-13b_ was first removed by antibiotic resistance mediated HR as described before. For _Kinesin-_

444 _13a_ and _-13c_, CRISPR mediated gene removal was utilised. 20 bp guide RNAs (gRNAs) targeting the

445 start and end of the gene were designed using CRISPOR (_http://crispor.tefor.net/_) (Figure S1A).

446 gRNAs were then integrated into a BsaI site of a vector carrying U6 promoter and RNA scaffold

447 (pCasGuide/pUC18) (Lopez-Obando et al., 2016; Collonnier et al., 2017), then the CRISPR cassettes

448 were cloned into a vector carrying nourseothricin resistance (pSY034) with InFusion to assemble

449 multiple gRNA cassettes into a plasmid (pSY062) following methods previously described (Leong et

450 al., 2018). Equal amounts of this circular multicassette plasmid and _Streptococcus pyogenes_ Cas9

451 expression vector (pGenius, (Collonnier et al., 2017)) were transformed into the _Kinesin-13b_ KO/EB1-

452 Citrine/mCherry-tubulin background. Confirmation of _Kinesin-13_ and _Kinesin-8_ KO lines (Figure

453 S1B–D) were carried out by PCR as previously described (Yamada et al., 2016; Leong et al., 2018).

454

455 _Endogenous C-terminal Citrine tagging_ C-terminal endogenous Kinesin-13 and -8 Citrine tagging lines

456 from (Miki et al., 2014) were used. In these lines, Kinesin-13 and -8 were tagged endogenously with

457 Citrine at the C-terminal via HR where 1 kb C-terminal sequence and the downstream sequence of stop

458 codon of the target gene flanking an antibiotic resistance cassette was used as the HR template.

459 Confirmation of this line was by PCR using primers designed to target the C-terminal region and

460 outside the 3'UTR of the target gene. To make rescue plasmids, Kinesin-13 sequence was cloned from

461 a cDNA library and ligated into the pENTR/D-TOPO vector. The Kinesin-13 mutant plasmids

462 (Kinesin-13b^{RIG}-Cerulean, Kinesin-13b$^{KVD/KEC}$-Cerulean, Kinesin-13b^{Loop12}-Cerulean) were generated

463 by mutagenesis with the full-length Kinesin-13 plasmid and primers listed in Table S2, S3. The cloned

464 Kinesin-13 sequences were ligated into pMN603 vector by a Gateway LR reaction, which contains

465 EF1α promoter, _Cerulean_ gene, nourseothricin-resistance cassette, _PTA1_ sequences designated for

466 homologous recombination mediated integration (Miki et al., 2016; Yoshida et al., 2019).

467

Imaging sample preparation

469 _Agar pad sample_ Moss samples used in time-lapse imaging were prepared either in 6-well glass

470 bottomed plates or 35 mm glass bottomed dishes as previously described (Yamada et al., 2016). Briefly,

471 protonema cells were plated onto glasses coated with BCD agar medium and culture for 4 to 6 d.

472

473   *Microdevice sample* Samples used for oblique illumination fluorescence microscopy were prepared in

474   BCD liquid medium in 15 µm height PDMS microfluidic chambers mostly following previously

475   described methods (Leong et al., 2018; Kozgunova and Goshima, 2019). Briefly, protonema cells were

476   homogenised in BCD liquid media, filtered through a sheet of 50 µm nylon-mesh, and injected into

477   microfluidic chambers attached unto 24 m x 32 mm micro cover glass (Matsunami, No. 1-S) and

478   cultured for 4 to 6 days.

479

480   *Calcofluor stained sample* 8-days-old moss colonies regenerated from single protoplasts were mounted

481   35 mm glass bottomed dishes with BCD agar medium. The moss colonies were stained with 100 µL of

482   0.1 mg/mL calcofluor solution diluted with water and covered with a cover glass. The samples were

483   then imaged with Nikon Eclipse TE2000-E inverted microscope

484

485   **Moss colony assay**

486   Protoplast regeneration assay was performed following the method described in (Vidali et al., 2007)

487   and (Yamada et al., 2016) with some modifications. In brief, sonicated moss on cellophane-lined

488   BCDAT plate was digested by 8% mannitol solution supplemented with 2% driselase. Generated

489   protoplasts were washed three times with 8% mannitol solution, and 1.5×10^5 mL^{-1} cells were

490   resuspended with 7ml of protoplast regeneration liquid. After overnight incubation under the dark

491   condition, the protoplasts were centrifuged at 510 *g* for 2 min and resuspended in 4 ml PRM solution in

492   which $CaCl_2$ was added after autoclave. 0.5–1 ml out of 4 ml protoplast solution was spread on

493   cellophane-lined PRM plate. Then, protoplasts were cultured for 4 d and transferred to BCDAT plate,

494   followed by 4 d culture. The 8-days-old moss colonies were observed with a stereomicroscope.

495

496   **Live *in vivo* imaging**

497   Spinning disc confocal microscopy using 100x 1.45-NA lens and ImagEM camera (Hamamatsu

498   Photonics) was performed with Nikon Ti inverted microscope as previously described (Yamada et al.,

499   2016). Z-series were taken using Nano-Z Series nanopositioner combined with a Nano-Drive controller

500   (Mad City Labs), where z-stack imaging was performed at 0.3 µm. Oblique illumination fluorescence

501   microscopy was carried out with a Nikon Ti microscope with a TIRF unit, a 100x 1.49-NA lens,

502   GEMINI split view (Hamamatsu Photonics), and EMCCD camera Evolve (Roper). Microscopes were

503   controlled by Micromanager or NIS-Elements (Nikon). Low magnification epifluorescence imaging

504   was carried out using Nikon Eclipse TE2000-E inverted microscope with 10x/0.3 LN1C Plain Fluo

505   lens and Zyla 5.5 sCMOS camera (Andor), controlled with IQ3 (Andor). Photobleaching experiments

506   were performed using an LSM780-DUO-NLO confocal microscopy system (Zeiss) using Plan-

15

507   Apochromat 63x/1.40 Oil DIC lens controlled using Zen (Zeiss) with 489 nM diode laser (time-lapse

508   imaging taken at 2 mW and bleaching at 100 mW). Moss expressing GFP-tubulin (GPH0438#30 for

509   *Kinesin-13* KO and *GFP-tubulin/histoneH2B-mRFP* for control) were used for photobleaching

510   experiments where images were acquired every 3 s. All imaging was performed at room temperature in

511   the dark. Moss colonies and gametophores were imaged with SMZ800N (Nikon) and ILCE-QX1

512   camera (SONY). The stereomicroscope system was controlled with PlayMemories software (SONY).

513

514   **Computer simulations**

515   Simulations were built in R (version 3.6.0)

516   (https://github.com/TomoyaEdzuka/MT_dyanamics_simulation). Parameters used in this simulation for

517   each condition (control or *Kinesin-13* KO) are listed in Table 1. In this simulation, catastrophe and

518   rescue frequency parameters were used to determine the probability of individual steps (1 s) undergoing

519   a transition change or to continue a growth/shrink phase. At each phase transition (i.e.

520   catastrophe/rescue event) new growth/shrink rates were assigned following a log normal distribution of

521   the growth and shrink parameters. MT lengths were then simulated for 4,000 trials (i.e. 4,000 MTs) for

522   240 steps (i.e. 4 min).

523

524   **Protein purification**

525   The motor domain of Kinesin-13b, which is the most highly expressed protein of the three paralogous

526   *Kinesin-13* genes, was cloned from moss cDNA and transgenically linked to monomeric GFP (mGFP)

527   and 6xHis at the C-terminus (plasmid pGG885, Table S2). Kinesin-13b^{motor}-mGFP expression was

528   induced in SOLBL21 *E. coli* with 0.1 mM IPTG for 20 h at 18 °C. Harvested cells were lysed using the

529   Advanced Digital Sonifier D450 (Branson) in lysis buffer (50 mM Tris-HCl [pH 8.0], 100 mM KCl, 2

530   mM MgCl$_2$, 20 mM imidazole, 0.1 mM ATP) supplemented with 10 mM β-mercaptoethanol and

531   protease inhibitors (1 mM PMSF and peptide inhibitor cocktail:5 mg/mL Aprotinin, 5 mg/mL

532   Chymostatin, 5 mg/mL Leupeptin, 5 mg/mL Pepstatin A). After rotation with nickel-NTA coated beads

533   for 2 h at 4 °C, the proteins were eluted using 500 µL elution buffer (50 mM Tris-HCl [pH 8.0], 100

534   mM KCl, 2 mM MgCl$_2$, 300 mM Imidazole, 0.1 mM ATP). Elution was repeated 5 to 7 times. The

535   eluates were then further purified through an AMPPNP-ATP 'binding-release' experiment. Eluates

536   were first bound with 1 mM AMPPNP to 76.5 µM of 1 mM GMPCPP-stabilised MTs, and sedimented

537   through an 80% glycerol cushion. Finally, the proteins were released from the pellet with 10 mM ATP.

538   The motor domain and nearby coiled-coil domain (residues 200-639) of Kinesin-8II was cloned from

539   moss cDNA and transgenically joined to GFP and 6xHis tag at the C-terminus (pTM266, Table S2),

540   and introduced into a pET-23 *E. coli* expression vector. The recombinant protein was purified from

541   SOLBL21 *E. coli* induced with 0.2 mM IPTG for 20 h at 18 °C. Harvested cells were lysed using the

16

542   Advanced Digital Sonifier D450 (Branson) in lysis buffer (25 mM MOPS [pH 7.0], 250 mM KCl, 2

543   mM MgCl$_2$, 5% sucrose, 30 mM imidazole, 0.1 mM ATP) supplemented with 5 mM β-

544   mercaptothanol and protease inhibitors (0.5 mM PMSF and peptide inhibitor cocktails). After rotation

545   with nickel-NTA coated beads (0.5 mL bed volume) for 2 h at 4 °C, proteins were eluted with 500 μL

546   elution buffer (25 mM MOPS [pH 7.0], 250 mM KCl, 2 mM MgCl$_2$, 400 mM imidazole, 5% sucrose,

547   1 mM ATP, 5 mM β-mercaptoethanol). Elution was repeated 5 to 7 times. Eluates were used

548   immediately. For the *in vitro* MT depolymerisation assay, the buffer for the elute was exchanged to 1x

549   Standard Assay Buffer (SAB: 25 mM MOPS [pH 7.0], 75 mM KCl, 2 mM MgCl$_2$, 1 mM EGTA)

550   supplemented with 1 mM ATP to remove imidazole using PD-25 column (GE Healthcare). *Drosophila*

551   KLP10A (plasmid pGG885) was purified referencing (Moriwaki and Goshima, 2016), and was

552   purified with the same protocol as Kinesin-13b^{motor}-mGFP. Instead of the 'binding-release' experiment,

553   elutes of KLP10A were subjected to buffer exchange to 1xMRB80 with 75 mM KCl and 0.1 mM ATP

554   using a PD-25 column (GE Healthcare). AtMIDD1 was purified following (Oda and Fukuda, 2013),

555   with some modifications. Briefly, GST-AtMIDD1 expression was induced in SOLBL21 *E. coli* using

556   0.2 mM IPTG, and cultured for 20 h at 18 °C. Harvested cells were lysed using the Advanced Digital

557   Sonifier D450 (Branson) in lysis buffer (10 mM HEPES [pH 7.4], 1 mM EGTA, 1 mM MgCl$_2$, 150

558   mM KCl) supplemented with 1 mM DTT and protease inhibitors (0.5 mM PMSF and peptide inhibitor

559   cocktails). After rotation with Glutathione Sepharose 4B beads (GE Healthcare, 0.5 mL bed volume)

560   for 2 h at 4 °C, proteins were eluted with 500 μL elution buffer (100 mM HEPES [pH 7.4], 100 mM

561   KCl, 30 mM reduced glutathione). Elution was repeated 5 to 7 times. Buffer was then exchanged using

562   a PD-10 column (GE Healthcare). Budding yeast Kip3 was purified following Kip3 purification (Gupta

563   et al., 2006) and *Drosophila* KLP67A purification (Edzuka and Goshima, 2019). In brief, ScKip3-

564   sfGFP-6xHis (pED273) was expressed in Sf21 moth cells at 27 °C for 72 h. Cells were lysed with 1%

565   Triton X-100 in lysis buffer (50 mM MOPS [pH 7.0], 250 mM NaCl, 2 mM MgCl$_2$, 1 mM EGTA, 20

566   mM imidazole, 0.1 mM ATP) supplemented with 2 mM β-mercaptothanol and protease inhibitors (0.5

567   mM PMSF and peptide inhibitor cocktails) for 30 min at 25 °C. After rotation with nickel-NTA coated

568   beads (0.5 mL bed volume) for 2 h at 4 °C, proteins were eluted with 500 μL elution buffer (25 mM

569   MOPS [pH 7.0], 250 mM KCl, 2 mM MgCl$_2$, 400 mM imidazole, 5% sucrose, 1 mM ATP, 5 mM β-

570   mercaptoethanol). Buffer was then exchanged to 1xSAB supplemented with 1 mM ATP to remove

571   imidazole using PD-25 column (GE Healthcare).

572

573   ***In vitro* MT depolymerisation**

574   The *in vitro* MT depolymerisation assay in (Moriwaki and Goshima, 2016) and (Gell et al., 2010) was

575   followed with some modifications. DmKLP10A, Kinesin-13b^{motor}-mGFP, AtMIDD1, and AtMIDD1

576   and Kinesin-13b^{motor}-mGFP were mixed with 30% Alexa Fluor-568 labelled GMPCPP-MT seeds

17

577 immobilised on silanised cover glass in assay buffer with (1x MRB80, 1 mM ATP, 50 mM glucose, 0.5

578 µg/µL κ-casein, 0.1% methylcellulose) supplemented with an oxygen scavenger system. Similarly,

579 Kinesin-8II[motor]-GFP and ScKip3 were also introduced to immobilised GMPCPP-MT seeds, but in a

580 different assay buffer (1xSAB, 0.1% methylcellulose, 50 mM glucose, 0.5 µg/µL κ-casein, 1 mM ATP,

581 75 mM KCl, supplemented with oxygen scavenger system). Proteins were used at 200 nM

582 concentrations, except AtMIDD1 which was used at 100 nM following (Oda and Fukuda, 2013). TIRF

583 imaging was taken every 3 s for 10 min at 25 °C.

584

585 ***In vitro* MT polymerisation assay**

586 We largely followed methods previously described (Li et al., 2012; Moriwaki and Goshima, 2016;

587 Leong et al., 2018) for the MT polymerisation assay. MT growth was initiated by flowing 20 µM

588 porcine brain tubulin (containing 10% Alexa Fluor 647-labelled tubulin) and 0, 0.15, 0.3, 0.6, and 1.5

589 µM purified Kinesin-13b[motor]-mGFP in assay buffer (1x MRB80, 75 mM KCl, 1 mM ATP, 50 nM

590 glucose, 1 mM GTP, 0.8 µg/µL κ-casein, 0.1% methylcellulose) supplemented with an oxygen

591 scavenger system. TIRF imaging of Alexa Fluor-568 labelled GMPCPP-MT seeds and Alexa Fluor-

592 647 labelled free tubulin was taken every 3 s for 10 min at 25 °C. Kymographs were drawn for 25

593 trackable dynamic MTs, and were analysed for catastrophe events and rescue events. Catastrophe

594 frequency was then defined by the number of catastrophe events per growth time (min), whereas rescue

595 frequency was defined by the number of rescue event per shrink time (min). Growth and shrink rates

596 were taken from the corresponding slopes from the same kymographs. Three independent experiments,

597 each with a different batch of purified proteins were performed.

598

599 ***In vitro* MT gliding assay**

600 For the gliding assay with purified Kinesin-8II[motor]-GFP, methods described in (Miki et al., 2015) were

601 referenced. Briefly, 10 µL of the freshly purified recombinant protein was introduced into the flow

602 chamber and incubated at room temperature for 2 min in the dark, then washed with 20 µL 1x Standard

603 Assay Buffer (SAB: 25 mM MOPS [pH 7.0], 75 mM KCl, 2 mM MgCl$_2$, 1 mM EGTA). Then 10 µL

604 reaction mix (1xSAB, 0.1% methylcellulose, 50 mM glucose, 0.5 µg/µL κ-casein, 50 mM GMPCPP-

605 MT seeds, 75 mM KCl, supplemented with oxygen scavenger system and varying concentrations of

606 ATP) was introduced into the flow chamber, and it was sealed with candle wax. TIRF imaging of

607 Alexa Fluor-647 labelled GMPCPP-MT seeds in *in vitro* MT gliding assays with Kinesin-8II[motor]-GFP

608 at varying ATP concentrations addition was taken every 3 s for 10 min at 23–25 °C. Kymographs were

609 drawn for 30~50 trackable dynamic MTs per sample, and the slopes of the kymographs were taken as

610 gliding velocity.

611

Data analysis

Moss colony growth rate GPH0438#30 (*Kinesin-13* KO) and GPH0002#5 (control) protoplasts were made following (Yamada et al., 2016) with some modifications. In brief, moss was incubated with 2% driselase solution (in 8% mannitol), washed thrice with 8% mannitol, incubated overnight in protoplast liquid medium, and then plated in PRM/T medium on cellophane-lined PRM plates, cultured at 25 °C under continuous light. On day 2, moss-lined cellophane was transferred to BCDAT plates. Around day 7 when individual colonies were larger, they were picked and inoculated on BCDAT plates, and cultured at 25 °C under continuous light. On day 27–28, images of plates with grown colonies were taken with the in-built camera of Xperia X Performance (23 MP Type 1/2.3' Exmor RS sensor, 24 mm equivalent lens with f/2.0 aperture). Images were analysed with FIJI, where images were first converted to 8-bit, automatically thresholded, and binarised. Colonies were automatically outlined with the wand tool and resulting area was obtained. Data in Figure 2B is pooled from three independent experiments.

Non-apical cell length Low magnification calcofluor stained images of moss colonies were used to measure non-apical cell length (see Figure 2E cartoon), where only caulonema cells were measured. To distinguish between caulonema and chloronema cells, protonema filaments were first judged by sight in bright field images of the same colonies, in which chloroplast density was used as an indicator of cell state (caulonema, chloroplast sparse; chloronema, chloroplast dense).

Branching distance, branch filament length, and branching angle Low magnification images of 8-days-old moss colonies regenerated from single protoplasts were used to analyse branching pattern parameters. Branching parameters were manually measured as shown in cartoon Figure 2E.

Nuclear movement velocity Samples from epifluorescence imaging of moss protonema filaments undergoing mitosis were analysed. Kymographs were drawn on the filaments, and nuclear movement velocity was obtained from the slopes of nuclear movement in these kymographs where positive and negative values were assigned to apical and basal directions, respectively.

Subapical cell length Samples from epifluorescence imaging of moss protonema filaments undergoing mitosis were analysed. Kymographs were drawn on the filaments, and the lengths from the middle of the spindle at anaphase to the cell tip and to the previous cell plate was measured as apical and subapical cell length, respectively (see Figure 3E cartoon).

646   *GFP-tubulin intensity around the nucleus* Spinning disc confocal fluorescence time-lapse imaging of

647   GFP-tubulin and histoneH2B-mRFP moss taken every 1 min was used for analysis. Segmented line

648   built-in tool in FIJI was used to mark the hemispheric circumference around the nucleus on the apical

649   and basal side at 1 min before NEBD (see Figure 4B cartoon) and mean pixel intensity was measured.

650   Apical:basal GFP-intensity ratio was defined as the ratio of the mean pixel intensity of the apical

651   hemisphere over that of the basal hemisphere.

652

653   *Mitotic duration* Mitosis images taken every 1 min with spinning disc confocal microscope were used

654   for analysis. Mitotic duration was defined as time from NEBD to anaphase onset, whereas

655   prometaphase is the time from NEBD to chromosome alignment, and metaphase duration is the time

656   from chromosome alignment to anaphase onset.

657

658   *Spindle length* Mitosis images taken every 1 min with spinning disc confocal microscope were used for

659   analysis. The metaphase spindle (defined as 1 min before anaphase onset) was used to analyse spindle

660   area. 4 points (the two limits of basal and apical pole widths) were marked and their (x, y) positions

661   were obtained, where spindle length was obtained from the distance between the midpoints of the basal

662   and apical pole widths.

663

664   *Spindle MT flux rate* Mitosis images were taken every 3 s with LSM780-DUO-NLO confocal

665   microscope. *Kinesin-13* KO (GPH0438#30) and control (*GFP-tubulin/histoneH2B-mRFP*) mitosis

666   were used for analysis. Cells were bleached along the equator of the mitotic spindle shortly after NEBD

667   once the spindle shape was formed, before anaphase entry. 38-pixel width slices covering the length of

668   the spindle were cut out and arranged using the montage tool in FIJI for easy viewing of the movement

669   of the bleached region, where their slopes were then taken as MT flux rate.

670

671   *Protonema filament bend frequency* Epifluorescence images of moss protonema filaments cultured on

672   BCDAT media were used for analysis in FIJI. Contrast was adjusted to make edges of protonema

673   filaments clearer. A blind test was performed to ascertain waviness threshold, where acute angles above

674   18° were determined to be 'wavy'. Randomly chosen protonema filaments were analysed for all the

675   angles of bends along a length of protonema filament using the FIJI in-built angle tool. The number of

676   bends that were 'wavy' (>18°) were counted, and taken over the length measured as bend frequency.

677

678   *MT foci trajectories* The MT foci of *Kinesin-13* KO, *-8* KO, and control moss expressing GFP-tubulin

679   were imaged at 60x magnification with z-series every 0.3 μm for a range of 20 μm every 3 min for 3 h.

680   Maximum z-projection of the files were analysed using FIJI MOSAIC plug-in (Sbalzarini and

20

681   Koumoutsakos, 2005) particle tracker 2D/3D (radius: 20, cut-off: 0.001, per/abs: 0.005, link range: 5,

682   displacement: 20, dynamics: Brownian) to automatically generate the MT foci trajectories. The linear

683   regression of the trajectories was rotated to horizontal and normalised to start at $(x, y) = (0, 0)$ in order to

684   plot graphs in Figure 5D.

685

686   *Interphase endoplasmic MT plus-end dynamics* For plus-end shrink rate, catastrophe frequency, and

687   rescue frequency, oblique illumination time-lapse images taken every 3 s of the interphase endoplasmic

688   MT network of *Kinesin-13* KO (GPH0438#30) and control (*GFP-tubulin/histoneH2B-mRFP*) were

689   analysed. For MT shrink rate, kymographs were drawn on five randomly chosen MTs per cell (cell N =

690   25; total MT N = 125), and the slope was taken as shrink rate. To analyse catastrophe and rescue

691   frequencies, ~5 x 6 μm area in a cell was randomly selected whereupon every traceable MT plus-end

692   was traced for a kymograph to count the number of catastrophe or rescue events over the observed

693   growth or shrink time respectively. For ease of tracking, areas with fewer MTs but were not near the

694   cell plate were preferred. Two independent experiments were performed and consistent. To determine

695   MT growth rate, *Kinesin-13* KO moss expressing EB1-Citrine was used, where Citrine marks growing

696   MT plus-ends. Spinning disc time-lapse images taken every 3 s of the interphase endoplasmic MT array

697   in *Kinesin-13* KO (GPH0577#2, 11) and control (*EB1-Citrine/mCherry-tubulin*, GPH0379#2) moss

698   were analysed. Kymographs were taken along the edge of the apical side of the tip cell of protonema

699   filaments. Slopes of EB1-Citrine comets in kymographs were measured and taken as growth rate.

700

701   *Statistics* Welch's two-sample t-test (two-sided) was used when samples were approximately normally

702   distributed. Tukey multiple comparison test was used for Figure 5B. Significance with the following p-

703   values are indicated as follows: *: < 0.05; **: < 0.01; ***: < 0.001; ****: < 0.0001.

704

705 **Accession numbers**

706   *Physcomitrella patens Kinesin-13a*, Pp3c1_27370; *Kinesin-13b*, Pp3c14_9830; *Kinesin-13c*,

707   Pp3c10_106980; *Kinesin-8Ia*, Pp3c1_32120; *Kinesin-8Ib*, Pp3c2_3070; *Kinesin-8II*, Pp3c21_9290.

708

709 **Author contributions**

710   MY and GG conceived project; SYL and MY designed and performed experiments; SYL, TE, and

711   MY analysed experimental data; TE performed computer simulation; SYL, GG, and MY wrote paper.

712

713 **Acknowledgements**

720

Figure legend

722 Figure 1: Conservation of Kinesin-13 and Kinesin-8 in the moss *Physcomitrella patens*.

723 (A) Protein domains of Kinesin-13 (represented with Kinesin-13b) and Kinesin-8 (represented with

724 Kinesin-8II) of moss, compared against *Drosophila melanogaster* KLP10A/Kinesin-13 and budding

725 yeast *Saccharomyces cerevisiae* Kip3/Kinesin-8. Domains of *Drosophila* and budding yeast proteins

726 were referenced from UniProt, whereas moss protein domains were predicted using InterPro.

727 (B, C) Kinesin-13 and -8 phylogeny across the moss *Physcomitrella patens*, the Brassicaceae

728 *Arabidopsis thaliana*, the liverwort *Marcantia polymorpha*, the rice *Oryza sativa* subspecies *Japonica*,

729 the fruit fly *Drosophila melanogaster*, mammalians *Mus muculus* and *Homo sapiens*, and also for

730 Kinesin-8 in budding yeast *Saccharomyces cerevisiae* and fission yeast *Schizosaccharomyces pombe*.

731 After amino acid sequences were aligned with MAFFT, gapped regions were removed manually using

732 MacClade. The phylogenetic tree was constructed using neighbour-joining methods using the Molecular

733 Evolutionary Genetics Analysis (MEGA) software. Reliability was assessed with 1,000 bootstrapping

734 trials. Protein sequences are presented in supplemental dataset. Horizontal branch length is proportional

735 to the estimated evolutionary distance. Bar, 0.1 amino acid substitution per site.

736

737 Figure 2: *Kinesin-13* and *-8* KO mosses are morphologically normal, but *Kinesin-13* KO moss shows

738 retarded growth and reduced cell length.

739 (A, B) Colony size comparison between control (*GFP-tubulin/histoneH2B-mRFP*) and *Kinesin-13* KO

740 (GPH0438#30, left) or *Kinesin-8* KO (GPH0433#9, right) moss. Colonies were cultured from single

741 protoplasts for 27-28 days on BCDAT where at least two independent experiments each with at least 2

742 plates of colonies were performed. The average colony area for each line on each plate was obtained.

743 Actual areas were then divided by the average area of the control sample to get relative colony size. In

744 the *Kinesin-13* KO experiment, KO moss had a relative size of 0.55 ± 0.04 (mean $\pm$ SEM; N = 7)

745 whereas control had a relative size of 1.00 ± 0.12 (mean $\pm$ SEM; N = 6). In the *Kinesin-8* KO

746 experiment, KO moss had a relative size of 1.01 ± 0.05 (mean $\pm$ SEM; N = 8) whereas control had a

747 relative size of 1.00 ± 0.08 (mean $\pm$ SEM; N = 8). Points represent individual colonies, results are from

748 one of at least two independent experiment. Bar, 5 mm.

749   (C) Gametophore and rhizoids of control (*GFP-tubulin/histoneH2B-mRFP*) and *Kinesin-13* KO

750   (GPH0438#6) or *Kinesin-8* KO (GPH0433#7) moss. Gametophores were isolated from colonies from

751   small colony subcultures cultured on BCDAT for 27-28 days. Bar, 1 mm.

752   (D) Day-8 moss colonies cultured from protoplast of control (*GFP-tubulin/histoneH2B-mRFP*) and

753   *Kinesin-13* KO (GPH0438#30) under brightfield light (top) and with calcofluor staining (bottom).

754   Yellow dashes boxes, inset region; bars, 500 μm; inset bar, 50 μm.

755   (E) Cartoon depicting the measurements taken for non-apical cell length in (F) and branching phenotype

756   analysis in (G).

757   (F) Non-apical cell lengths of caulonema filaments were measured using calcofluor stained colonies as in

758   (D, bottom) for control (*GFP-tubulin/histoneH2B-mRFP*) and *Kinesin-13* KO (GPH0438#30). Non-

759   apical cell length was reduced in *Kinesin-13* KO moss to 79.9 ± 5.5 μm (mean $\pm$ SEM; N = 43),

760   compared to control moss of 113.7 ± 1.9 μm (mean $\pm$ SEM; N = 132). Points represent individual cells;

761   results are pooled from two independent experiments where two independent lines were analysed.

762   (G) Branching phenotype analysis of control (*GFP-tubulin/histoneH2B-mRFP*) and *Kinesin-13* KO

763   (GPH0438#30). In particular, branching distance of the first branch site to cell tip (top graph, leftmost

764   bars) was increased in *Kinesin-13* KO moss to 338.4 ± 12.9 μm (mean $\pm$ SEM; N = 55), compared to

765   control moss of 293.1 ± 8.8 μm (mean $\pm$ SEM; N = 71). Points represent individual filaments; results are

766   pooled from two independent experiments where two independent lines were analysed.

767

768   Figure 3: *Kinesin-13s contribute to* triple KO moss shows retrograde nuclear movement not seen in

769   single KOs, but manifests in to a lesser degree in the *Kinesin-13ac* double KO line.

770   (A) Snapshots of control (*GFP-tubulin/histoneH2B-mRFP*) and *Kinesin-13* KO (GPH0438#30) moss

771   during prophase nuclear/spindle movement. *Kinesin-13* KO moss shows retrograde nuclear/spindle

772   movement. Apical side, right, positive value for analysis in (B) and (D); basal side, left, negative values

773   for analysis in (B) and (D); yellow dotted line, nucleus position at NEBD; bar, 50 μm; NEBD, 0 min.

774   (B) Nuclear movement velocity during prophase of control (*GFP-tubulin/histoneH2B-mRFP*; $0.68 \pm$

775   0.10 μm/min, mean $\pm$ SEM; N = 8), *Kinesin-13a* single KO (GPH0411#43; 0.85 ± 0.10 μm/min, mean

776    $\pm$ SEM; N = 8), *Kinesin-13b* single KO (GPH0412#11; 0.43 ± 0.03 μm/min, mean $\pm$ SEM; N = 7),

777   *Kinesin-13ab* double KO (GPH0419#33; 0.62 ± 0.04 μm/min, mean $\pm$ SEM; N = 11), *Kinesin-13ac*

778   double KO (GPH0420#125; -0.03 ± 0.13 μm/min, mean $\pm$ SEM; N = 16), and *Kinesin-13abc* triple KO

779   (GPH0438#30; -0.69 ± 0.08 μm/min, mean $\pm$ SEM; N = 11). *Kinesin-13abc* triple KO shows a clear

780   retrograde nuclear movement, whereas *Kinesin-13ac* double KO shows intermediate retrograde nuclear

781   movement. Apically directed movement, positive values; basally directed movement, negative values.

23

782   represent individual mitotic events. Results are from one of three independent experiments where two

783   independent lines were analysed.

784   (C) Protein domains of Kinesin-13b and mutant proteins for rescue experiments. Point mutations on

785   Kinesin-13b-Cerulean which was introduced under the *EF1α* promoter at the *PTA1* site in the moss used

786   for rescue experiments are illustrated.

787   (D) Nuclear movement velocity during prophase of control (*GFP-tubulin/histoneH2B-mRFP*; 0.94 ±

788   0.10 μm/min, mean ± SEM; N = 17), *Kinesin-13abc* triple KO (GPH0438#30; -1.43 ± 0.22 μm/min,

789   mean ± SEM; N = 29), *Cerulean/Kinesin-13abc* triple KO (GPH0903#1; -0.99 ± 0.25 μm/min, mean ±

790   SEM; N = 16), *Kinesin-13b(FL)-Cerulean/Kinesin-13abc* triple KO (GPH0899#10; 1.04 ± 0.09

791   μm/min, mean ± SEM; N = 13), *Kinesin-13b^{RIG}-Cerulean/Kinesin-13abc* triple KO (GPH0902#2; -0.58

792   ± 0.20 μm/min, mean ± SEM; N = 17), *Kinesin-13b$^{KVD/KEC}$-Cerulean/Kinesin-13abc* triple KO

793   (GPH0900#4; -0.94 ± 0.08 μm/min, mean ± SEM; N = 10), and *Kinesin-13b^{Loop2}-Cerulean/Kinesin-*

794   *13abc* triple KO (GPH0901#1; -1.05 ± 0.20 μm/min, mean ± SEM; N = 27). Apically directed

795   movement, positive values; basally directed movement, negative values. Points represent individual

796   mitotic events. Results are from one of two independent experiments where at least two independent

797   lines were analysed.

798   (E) Cartoon depicting how subapical and apical cell lengths were measured for (F).

799   (F) Subapical cell length was reduced in the *Kinesin-13* KO line (GPH0438#30; 70.9 ± 3.6 μm (mean ±

800   SEM; N = 26; p-value < 0.05)) compared to the control (*GFP-tubulin/histoneH2B-mRFP*; 105.2 ± 12.4

801   μm (mean ± SEM; N = 11)). Each point represents individual mitotic events. Results shown are from

802   one of two independent experiments where two independent lines were analysed.

803

804   <u>Figure 4: *Kinesin-13* KO moss shows defects in nuclear-proximal MT array, mitotic duration, and</u>

805   <u>spindle length, but shows no difference in spindle flux rate.</u>

806   (A) Mitosis of control (*GFP-tubulin/histoneH2B-mRFP*), *Kinesin-13* KO (GPH0438#6), and *Kinesin-8*

807   KO (GPH0433#9) moss. *Kinesin-13* KO showed reduced metaphase spindle length, retrograde nuclear

808   movement during prophase, increased mitotic duration, and loss of apical bias of nuclear-MTs. *Kinesin-8*

809   KO did not show mitotic defects. Bar, 10 μm; NEBD, 0 min; left, basal side; right, apical side.

810   (B, C) Apical:basal GFP-intensity ratio of GFP-tubulin around the nucleus 1 min before NEBD was

811   measured as the ratio of GFP-tubulin intensities between apical and basal hemispheric circumference.

812   Control (*GFP-tubulin/histoneH2B-mRFP*), 1.17 ± 0.04 (mean ± SEM; N=9; p-value < 0.05); *Kinesin-13*

813   KO (GPH0438#6, 30), 1.00 ± 0.07 (mean ± SEM; N = 10). Points represent individual mitotic events.

814   (D) Mitotic duration of control (*GFP-tubulin/histoneH2B-mRFP*), *Kinesin-13* KO (GPH0438#6, 30),

815   and *Kinesin-8* KO (GPH0433#7, 9) moss as measured from NEBD to anaphase onset. Control, 9.8 ± 0.3

24

816   min (mean ± SEM; N = 11); *Kinesin-13* KO, 11.8 ± 0.4 min (mean ± SEM, N = 15; p-value < 0.001).

817   *Kinesin-8* KO, 9.1 ± 0.2 min (mean ± SEM; N = 10; p-value < 0.05). The duration of prometaphase

818   (from NEBD to chromosome alignment) and metaphase (chromosome alignment to anaphase onset)

819   was also measured and shown. Data shown was pooled from two independent experiments.

820   (E) Spindle length was measured at metaphase (defined as 1 min before anaphase onset) by obtaining the

821   distance between midpoints of apical and basal spindle widths. Control (*GFP-tubulin/histoneH2B-*

822   *mRFP*), 13.0 ± 0.3 µm (mean ± SEM; N = 4); *Kinesin-13* KO (GPH0438#30), 11.2 ± 0.3 µm (mean ±

823   SEM; N = 10; p-value <0.01); *Kinesin-8* KO (GPH0433#9), 12.3 ± 0.5 µm (mean ± SEM; N = 10).

824   Points represent individual mitotic events.

825   (F) Spindle poleward flux of control (*GFP-tubulin/histoneH2B-mRFP*) and *Kinesin-13* KO

826   (GPH0438#30) moss was examined in photobleaching experiments where GFP-tubulin signals on a strip

827   along the metaphase plate was bleached. The bleached regions separating towards the poles are

828   indicative of spindle poleward flux function. Horizontal bar, 5 µm; vertical bar; 12 s; yellow dashed

829   rectangle in the top panel indicates region used to make time series (bottom panel); cyan dashed rectangle

830   represents bleached region; red lines indicate the segmented lines drawn on the kymograph to obtain flux

831   rate in (G).

832   (G) Quantification of spindle poleward flux experiment as shown in (F). Control, 2.1 ± 0.2 µm/min

833   (mean ± SEM; N = 22); *Kinesin-13* KO, 2.2 ± 0.4 µm/min (mean ± SEM; N = 19). Points represent

834   individual mitotic events, shown are results from four independent experiments.

835

836   Figure 5: *Kinesin-13* and *-8* KO moss have wavy protonema filaments correlated with unstable MT foci

837   positioning.

838   (A) Protonema filaments of control (*GFP-tubulin/histoneH2B-mRFP*), *Kinesin-13* KO (GPH0438#30),

839   *Kinesin-8* KO (GPH0433#9) moss. Bar, 50 µm.

840   (B) Waviness of protonema filaments measured as frequency of wavy bend (>18°) of protonema

841   filaments over measured lengths. Control (*GFP-tubulin/histoneH2B-mRFP*), 0.006 ± 0.001 µm^{-1} (mean

842   ± SEM; N = 28 filaments); *Kinesin-13* KO (GPH0438#30), 0.024 ± 0.002 µm^{-1} (mean ± SEM; N = 26

843   filaments; p-value < 0.0001); *Kinesin-8* KO (GPH0433#7), 0.022 ± 0.005 µm^{-1} (mean ± SEM; N = 8

844   filaments; p-value < 0.01); *Cerulean/Kinesin-13* KO (GPH0903#1), 0.022 ± 0.004 µm^{-1} (mean ± SEM;

845   N = 12); *Kinesin-13b(full-length)-Cerulean/Kinesin-13* KO (GPH0899#10), 0.004 ± 0.001 µm^{-1} (mean

846   ± SEM; N = 8; p-value < 0.0001). Points represent individual protonema filaments, results shown are

847   from one experiment of at least four independent experiments.

848   (C) MT foci at tip of caulonema cell of control (*GFP-tubulin/histoneH2B-mRFP*), *Kinesin-13* KO

849   (GPH0438#30), *Kinesin-8* KO (GPH0433#9) moss. Images were acquired with z-sections at 0.3 µm

850   intervals for 20 μm range, and maximum z-projections are displayed. Bottom panels show overlaid time

851   series. Bar, 10 μm; colours in time series indicate different time points as labelled in top panels.

852   (D) MT foci positions were tracked using FIJI MOSAIC plug-in 2D/3D particle tracker (Sbalzarini and

853   Koumoutsakos, 2005) in time-lapse imaging data as in (C). (x, y) trajectories of three representative MT

854   foci (shown in different colours) for each line are displayed. Each point represents subsequent positions

855   at each time point, at 3 min intervals for 3 h. Same lines as in (B) are represented.

856

857   Figure 6: *Kinesin-13* localises to the interphase MT network and depletion of *Kinesin-13* results in

858   increased shrink rate, reduced catastrophe frequency, increased rescue frequency, and reduced growth

859   rate.

860   (A) MT foci of *Kinesin-13c-Citrine/mCherry-tubulin* (GPH0100#15) moss. Image was acquired at 0.3

861   μm intervals for 10 μm range; shown is maximum z-projection. Bar, 5 μm.

862   (B) Interphase MT network of *Kinesin-13c-Citrine/mCherry-tubulin* (GPH0100#15) moss. Images were

863   acquired by oblique illumination fluorescence split-view microscopy to avoid chloroplast

864   autofluorescence. Bar, 2 μm.

865   (C) Kymograph of MT growth taken from imaging as in (B), taken every 3 s. Vertical bar, 2 min;

866   horizontal bar, 5 μm.

867   (D) Interphase MT plus-end shrink rate of control (*GFP-tubulin/histoneH2B-mRFP*, 0.245 ± 0.012 μm/s

868   (mean $\pm$ SEM; N = 25 cells)) and *Kinesin-13* KO (GPH0438#30, 0.429 ± 0.021 μm/s (mean $\pm$ SEM; N

869   = 25 cells; p-value < 0.0001)) moss. Points represent individual cells; results shown are from one

870   experiment of two independent experiments.

871   (E) Interphase MT catastrophe frequency of control (*GFP-tubulin/histoneH2B-mRFP*, 9.3 ± 1.2 x10^{-3}/s

872   (mean $\pm$ SEM; N = 33 cells)) and *Kinesin-13* KO (GPH0438#30, 2.2 ± 0.5 x10^{-3}/s (mean $\pm$ SEM; N =

873   28 cells; p-value < 0.0001)). Points represent individual cells; results shown are from two independent

874   experiments.

875   (F) Interphase MT rescue frequency of control (*GFP-tubulin/histoneH2B-mRFP,* 14 ± 3 x10^{-3}/s (mean $\pm$

876   SEM; N = 25 cells)) and *Kinesin-13* KO (GPH0438#30, 25 ± 6 x10^{-3}/s (mean $\pm$ SEM; N = 23 cells)).

877   Points represent individual cells; results shown are from two independent experiments.

878   (G) Interphase MT plus-end growth rate of control (*EB1-Citrine/mCherry-tubulin*, GPH0379#2, $0.147 \pm$

879   0.013 μm/s (mean $\pm$ SEM; N = 5 cells, 50 MTs)) and *Kinesin-13* KO moss (GPH0577#11, $0.093 \pm$

880   0.003 μm/s (mean $\pm$ SEM; N = 5 cells, 50 MTs; p-value < 0.05)). Points represent individual cells.

881   (H) Simulation of MT growth of 4,000 MTs in 4 min based on a probability model established using MT

882   dynamics parameters from *in vivo* interphase MT dynamics analyses (D–G) (refer to Materials &

883   Methods, and Table 1). Control MT dynamics parameters yielded approximately normal distributions of

884 MT lengths and tended to have a larger population of MTs with longer lengths, with the longest 25% of

885 MTs ranging between 23.4 to 59.8 µm in length. For MTs under *Kinesin-13* KO conditions, the

886 distribution of MT length was narrower, with 50% of all MTs between 11.5 to 22.6 µm lengths, whereas

887 the longest 25% of MTs ranged from 22.6 to 29.4 µm in length. Histogram bin width = 0.5 µm.

888

889 Figure 7: Recombinant Kinesin-13 does not depolymerise stabilised GMPCPP-MT seeds but shows MT

890 catastrophe inducing activity.

891 (A) Protein domains of Kinesin-13b and recombinant Kinesin-13b^{motor}-mGFP construct. Protein

892 domains were determined using InterPro. His-tag for affinity purification was attached to C-terminus of

893 the recombinant protein.

894 (B) *In vitro* MT depolymerisation assay using GMPCPP-stabilised MT seeds was performed using

895 purified DmKLP10A, recombinant Kinesin-13b^{motor}-mGFP construct, AtMIDD1, AtMIDD1 and

896 Kinesin-13b^{motor}-mGFP construct, and also under buffer only conditions. Only DmKLP10A

897 successfully depolymerised MT seeds. The slight reduction in intensity in the bottom panels is due to

898 photobleaching during imaging. All proteins were used at 200 nM except for AtMIDD1 which was at

899 100 nM. Bar, 5 µm.

900 (C) Representative kymographs of *in vitro* MT dynamics polymerisation assays with Kinesin-13b^{motor}-

901 mGFP construct at 0, 0.3, and 1.5 µM. Time-lapse imaging was performed with TIRF microscopy

902 taken every 3 s. Brightness and contrast was manually adjusted. Vertical bar, 2 min; horizontal bar; 5

903 µm.

904 (D-G) *In vitro* MT dynamics parameters were analysed from time-lapse imaging of *in vitro* MT

905 dynamics polymerisation assays with Kinesin-13b^{motor}-mGFP construct at 0, 0.15, 0.3, 0.6, and 1.5 µM

906 taken using TIRF microscopy at every 3 s. In particular, growth rate was observed to reduce slightly,

907 from 9.0 ± 0.4 x10^{-3}µm/s (mean $\pm$ SEM; N = 3) in buffer only conditions, to 7.5 ± 0.7 x10^{-3}µm/s (mean

908 $\pm$ SEM; N = 3) in 1.5 µM protein. Catastrophe frequency was observed to reproducibly increase with

909 high concentrations of Kinesin-13b^{motor}-mGFP, having a catastrophe frequency of 2.3 ± 0.2 x10^{-3}/s

910 (mean $\pm$ SEM; N = 3) at 1.5 µM protein, compared to 1.2 ± 0.3 x10^{-3}/s in buffer only conditions. Points

911 represent mean values from independent experiments.

912

913 Figure 8: Recombinant Kinesin-8 motor does not depolymerise MTs but shows MT gliding activity.

914 (A) Protein domains of Kinesin-8II and recombinant Kinesin-8II^{motor}-GFP construct. Protein domains

915 were identified using InterPro. His-tag for affinity purification was attached to C-terminus of the

916 recombinant protein.

917 (B) *In vitro* MT depolymerisation assay using GMPCPP-stabilised MT seeds was performed using

918 purified ScKip3, recombinant Kinesin-8II^{motor}-GFP, and also under buffer only conditions. Only

27

919   ScKip3 showed MT depolymerisation activity. The slight reduction in intensity in bottom panels is due

920   to photobleaching during imaging. All proteins were used at 200 nM. Bar, 10 μm.

921   (C) ATP-dependent MT gliding velocity of Kinesin-8II^{motor}-GFP. 1 mM ATP, 0.68 ± 0.03 μm/min

922   (mean $\pm$ SEM; N = 124 MTs); 5 mM ATP, 1.18 ± 0.02 μm/min (mean $\pm$ SEM; N = 121 MTs, p-value

923   < 0.0001).

924   (D) *In vitro* MT gliding assay using GMPCPP-stabilised MTs on Kinesin-8II^{motor}-GFP which was

925   immobilised on glass, at 0, 1, and 5 mM ATP. Red dotted line in top panel indicates segmented line

926   used to draw kymographs (bottom panels). Gliding activity of Kinesin-8II^{motor}-GFP was verified in 3

927   independent experiments. Vertical bar, 45 s; horizontal bar, 2 μm.

928
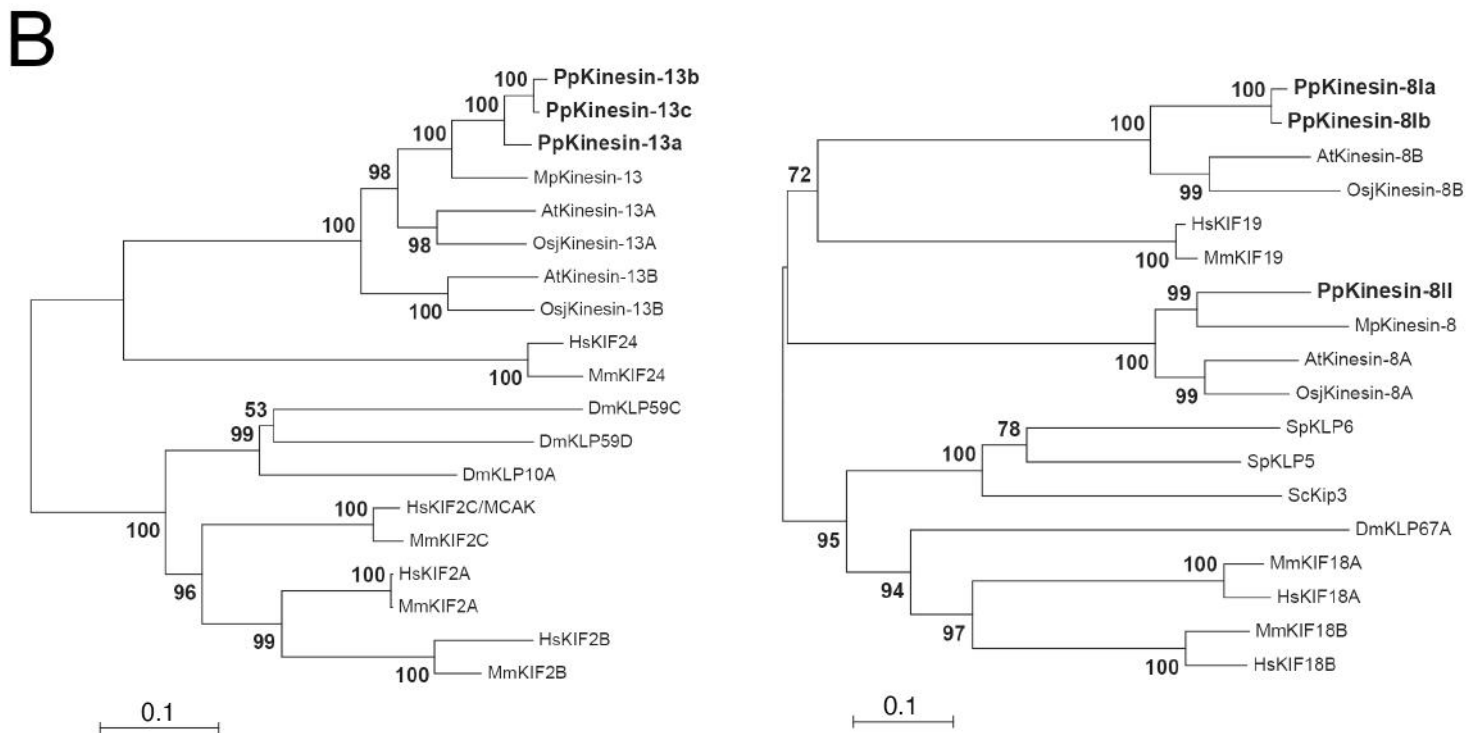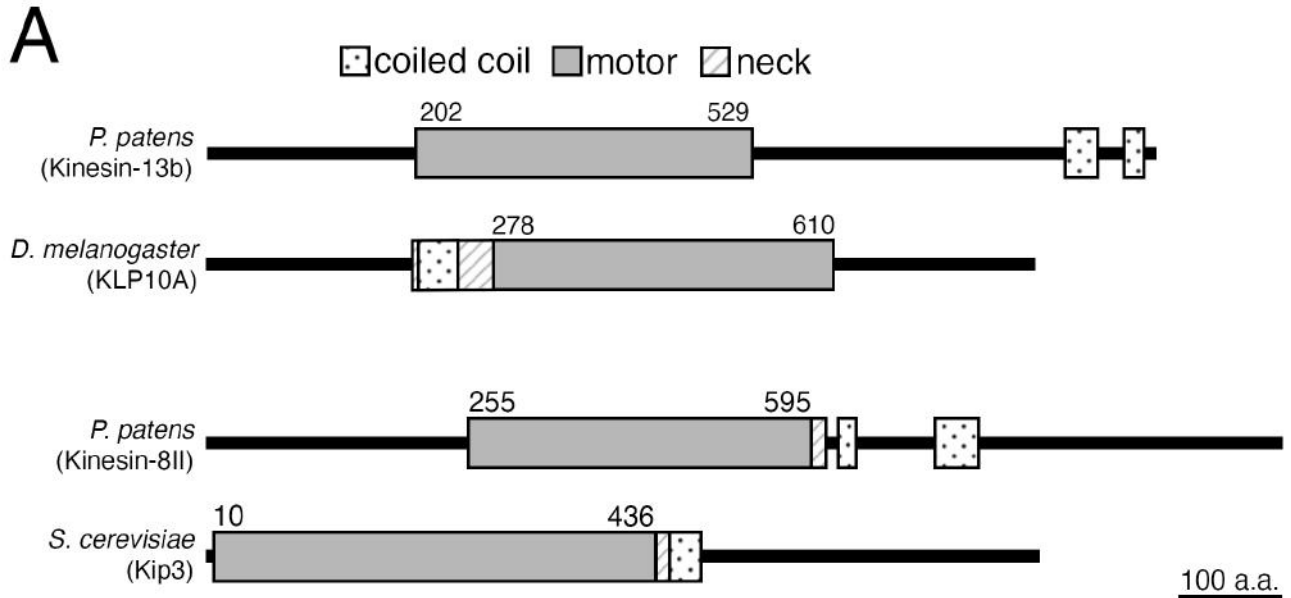
Figure 1

Figure 1: Conservation of Kinesin-13 and Kinesin-8 in the moss *Physcomitrella patens*.

(A) Protein domains of Kinesin-13 (represented with Kinesin-13b) and Kinesin-8 (represented with Kinesin-8II) of moss, compared against *Drosophila melanogaster* KLP10A/Kinesin-13 and budding yeast *Saccharomyces cerevisiae* Kip3/Kinesin-8. Domains of *Drosophila* and budding yeast proteins were referenced from UniProt, whereas moss protein domains were predicted using InterPro. **(B, C)** Kinesin-13 and -8 phylogeny across the moss *Physcomitrella patens*, the Brassicaceae *Arabidopsis thaliana*, the liverwort *Marcantia polymorpha*, the rice *Oryza sativa* subspecies *Japonica*, the fruit fly *Drosophila melanogaster*, mammalians *Mus muculus* and *Homo sapiens*, and also for Kinesin-8 in budding yeast *Saccharomyces cerevisiae* and fission yeast *Schizosaccharomyces pombe*. After amino acid sequences were aligned with MAFFT, gapped regions were removed manually using MacClade. The phylogenetic tree was constructed using neighbour-joining methods using the Molecular Evolutionary Genetics Analysis (MEGA) software. Reliability was assessed with 1,000 bootstrapping trials. Horizontal branch length is proportional to the estimated evolutionary distance. Protein sequences are presented in supplemental dataset. Bar, 0.1 amino acid substitution per site.

Figure 2
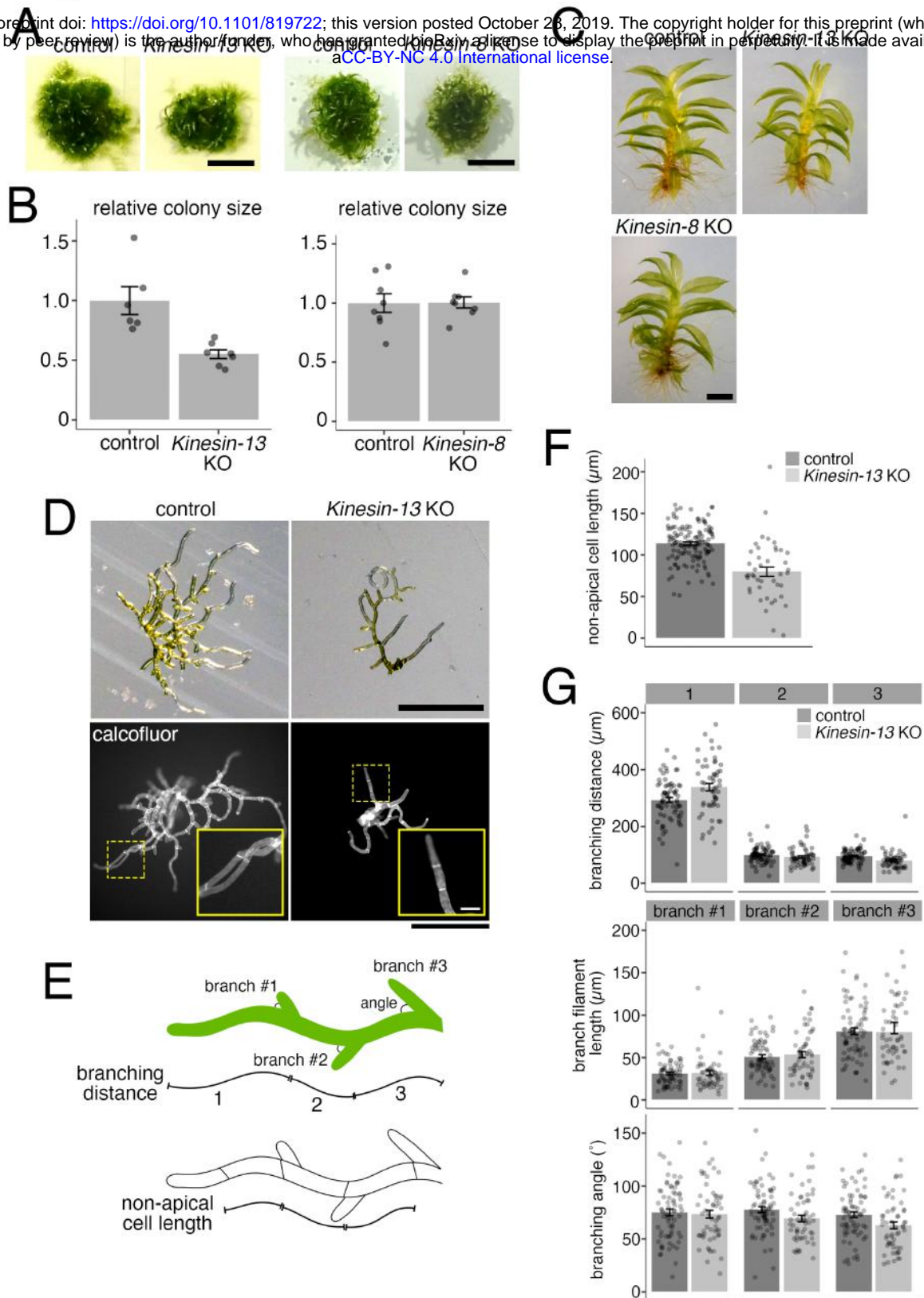
Figure 2: *Kinesin-13* and *-8* KO mosses are morphologically normal, but *Kinesin-13* KO moss shows retarded growth and reduced cell length.

(A, B) Colony size comparison between control (*GFP-tubulin/histoneH2B-mRFP*) and *Kinesin-13* KO (GPH0438#30, left) or *Kinesin-8* KO (GPH0433#9, right) moss. Colonies were cultured from single protoplasts for 27-28 days on BCDAT where at least two independent experiments each with at least 2 plates of colonies were performed. The average colony area for each line on each plate was obtained. Actual areas were then divided by the average area of the control sample to get relative colony size. In the *Kinesin-13* KO experiment, KO moss had a relative size of 0.55 ± 0.04 (mean ± SEM; N = 7) whereas control had a relative size of 1.00 ± 0.12 (mean ± SEM; N = 6). In the *Kinesin-8* KO experiment, KO moss had a relative size of 1.01 ± 0.05 (mean ± SEM; N = 8) whereas control had a relative size of 1.00 ± 0.08 (mean ± SEM; N = 8). Points represent individual colonies, results are from one of at least two independent experiment. Bar, 5 mm. **(C)** Gametophore and rhizoids of control (*GFP-tubulin/histoneH2B-mRFP*) and *Kinesin-13* KO (GPH0438#6) or *Kinesin-8* KO (GPH0433#7) moss. Gametophores were isolated from colonies from small colony subcultures cultured on BCDAT for 27-28 days. Bar, 1 mm. **(D)** Day-8 moss colonies cultured from protoplast of control (*GFP-tubulin/histoneH2B-mRFP*) and *Kinesin-13* KO (GPH0438#30) under brightfield light (top) and with calcofluor staining (bottom). Yellow dashes boxes, inset region; bars; 500 μm; inset bar, 50 μm. **(E)** Cartoon depicting the measurements taken for non-ap ical cell length in (F) and branching phenotype analysis in (G). **(F)** Non-apical cell lengths of caulonema filaments were measured using calcofluor stained colonies as in (D, bottom) for control (*GFP-tubulin/histoneH2B-mRFP*) and *Kinesin-13* KO (GPH0438#30). Non-apical cell length was reduced in *Kinesin-13* KO moss to 79.9 ± 5.5 μm (mean ± SEM; N = 43), compared to control moss of 113.7 ± 1.9 μm (mean ± SEM; N = 132). Points represent individual cells; results are pooled from two independent experiments where two independent lines were analysed. **(G)** Branching phenotype analysis of control (*GFP-tubulin/histoneH2B-mRFP*) and *Kinesin-13* KO (GPH0438#30). In particular, branching distance of the first branch site to cell tip (top graph, leftmost bars) was increased in *Kinesin-13* KO moss to 338.4 ± 12.9 μm (mean ± SEM; N = 55), compared to control moss of 293.1 ± 8.8 μm (mean ± SEM; N = 71). Points represent individual filaments; results are pooled from two independent experiments where two independent lines were analysed.

Figure 3
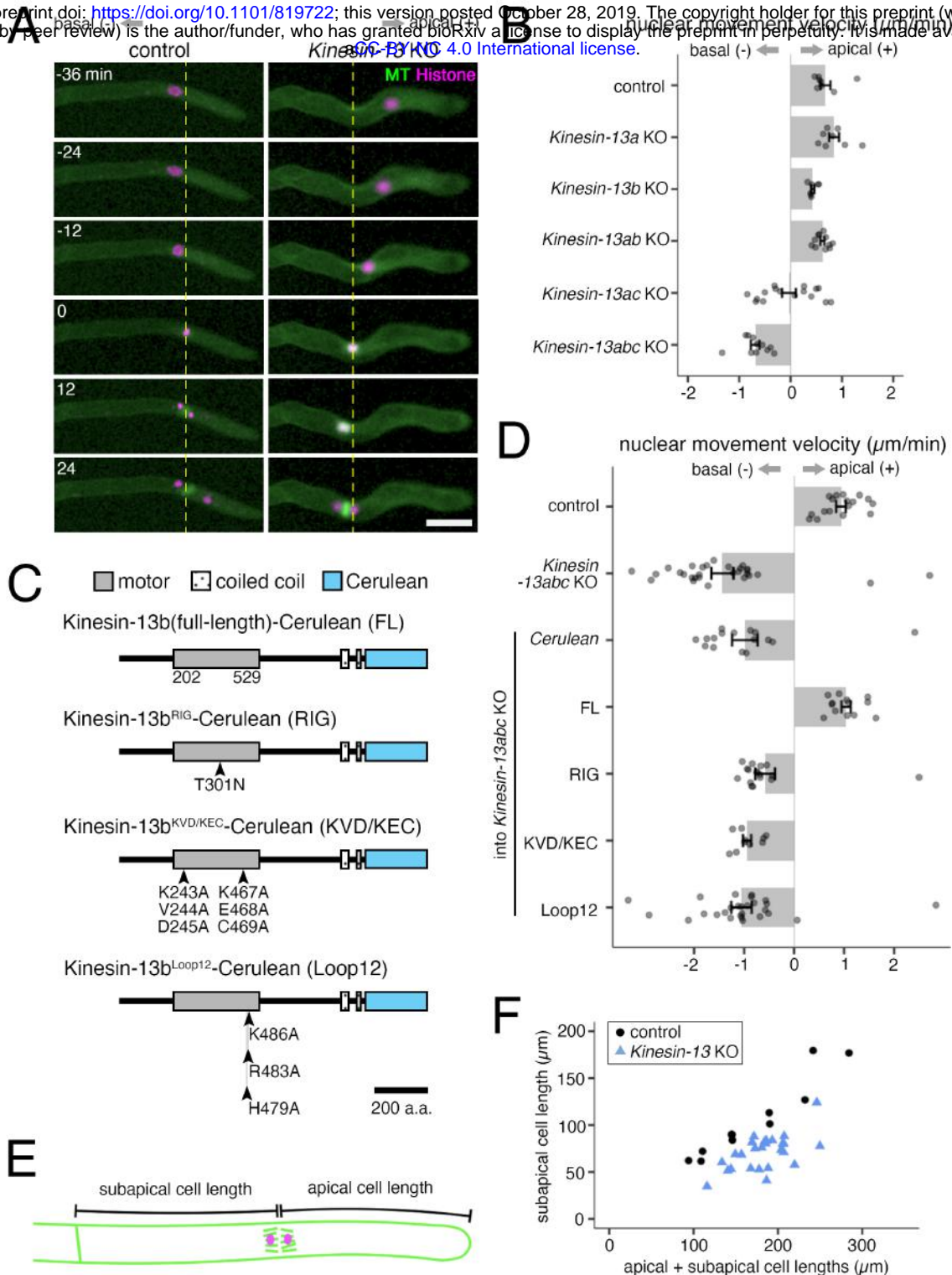
Figure 3: *Kinesin-13s contribute to* triple KO moss shows retrograde nuclear movement not seen in single KOs, but manifests in to a lesser degree in the *Kinesin-13ac* double KO line.

(A) Snapshots of control (*GFP-tubulin/histoneH2B-mRFP*) and *Kinesin-13* KO (GPH0438#30) moss during prophase nuclear/spindle movement. *Kinesin-13* KO moss shows retrograde nuclear/spindle movement. Apical side, right, positive value for analysis in (B) and (D); basal side, left, negative values for analysis in (B) and (D); yellow dotted line, nucleus position at NEBD; bar, 50 μm; NEBD, 0 min. **(B)** Nuclear movement velocity during prophase of control (*GFP-tubulin/histoneH2B-mRFP*; 0.68 ± 0.10 μm/min, mean ± SEM; N = 8), *Kinesin-13a* single KO (GPH0411#43; 0.85 ± 0.10 μm/min, mean ± SEM; N = 8), *Kinesin-13b* single KO (GPH0412#11; 0.43 ± 0.03 μm/min, mean ± SEM; N = 7), *Kinesin-13ab* double KO (GPH0419#33; 0.62 ± 0.04 μm/min, mean ± SEM; N = 11), *Kinesin-13ac* double KO (GPH0420#125; -0.03 ± 0.13 μm/min, mean ± SEM; N = 16), and *Kinesin-13abc* triple KO (GPH0438#30; -0.69 ± 0.08 μm/min, mean ± SEM; N = 11). *Kinesin-13abc* triple KO shows a clear retrograde nuclear movement, whereas *Kinesin-13ac* double KO shows intermediate retrograde nuclear movement. Apically directed movement, positive values; basally directed movement, negative values. represent individual mitotic events. Results are from one of three independent experiments where two independent lines were analysed. **(C)** Protein domains of Kinesin-13b and mutant proteins for rescue experiments. Point mutations on Kinesin-13b-Cerulean which was introduced under the *EF1α* promoter at the *PTA1* site in the moss used for rescue experiments are illustrated. **(D)** Nuclear movement velocity during prophase of control (*GFP-tubulin/histoneH2B-mRFP*; 0.94 ± 0.10 μm/min, mean ± SEM; N = 17), *Kinesin-13abc* triple KO (GPH0438#30; -1.43 ± 0.22 μm/min, mean ± SEM; N = 29), *Cerulean/Kinesin-13abc* triple KO (GPH0903#1; -0.99 ± 0.25 μm/min, mean ± SEM; N = 16), *Kinesin-13b(FL)-Cerulean/Kinesin-13abc* triple KO (GPH0899#10; 1.04 ± 0.09 μm/min, mean ± SEM; N = 13), *Kinesin-13b^RIG^-Cerulean/Kinesin-13abc* triple KO (GPH0902#2; -0.58 ± 0.20 μm/min, mean ± SEM; N = 17), *Kinesin-13b^KVD/KEC^-Cerulean/Kinesin-13abc* triple KO (GPH0900#4; -0.94 ± 0.08 μm/min, mean ± SEM; N = 10), and *Kinesin-13b^Loop2^-Cerulean/Kinesin-13abc* triple KO (GPH0901#1; -1.05 ± 0.20 μm/min, mean ± SEM; N = 27). Apically directed movement, positive values; basally directed movement, negative values. Points represent individual mitotic events. Results are from one of two independent experiments where at least two independent lines were analysed. **(E)** Cartoon depicting how subapical and apical cell lengths were measured for (F). **(F)** Subapical cell length was reduced in the *Kinesin-13* KO line (GPH0438#30; 70.9 ± 3.6 μm (mean ± SEM; N = 26; p-value < 0.05)) compared to the control (*GFP-tubulin/histoneH2B-mRFP*; 105.2 ± 12.4 μm (mean ± SEM; N = 11)). Each point represents individual mitotic events. Results shown are from one of two independent experiments where two independent lines were analysed.
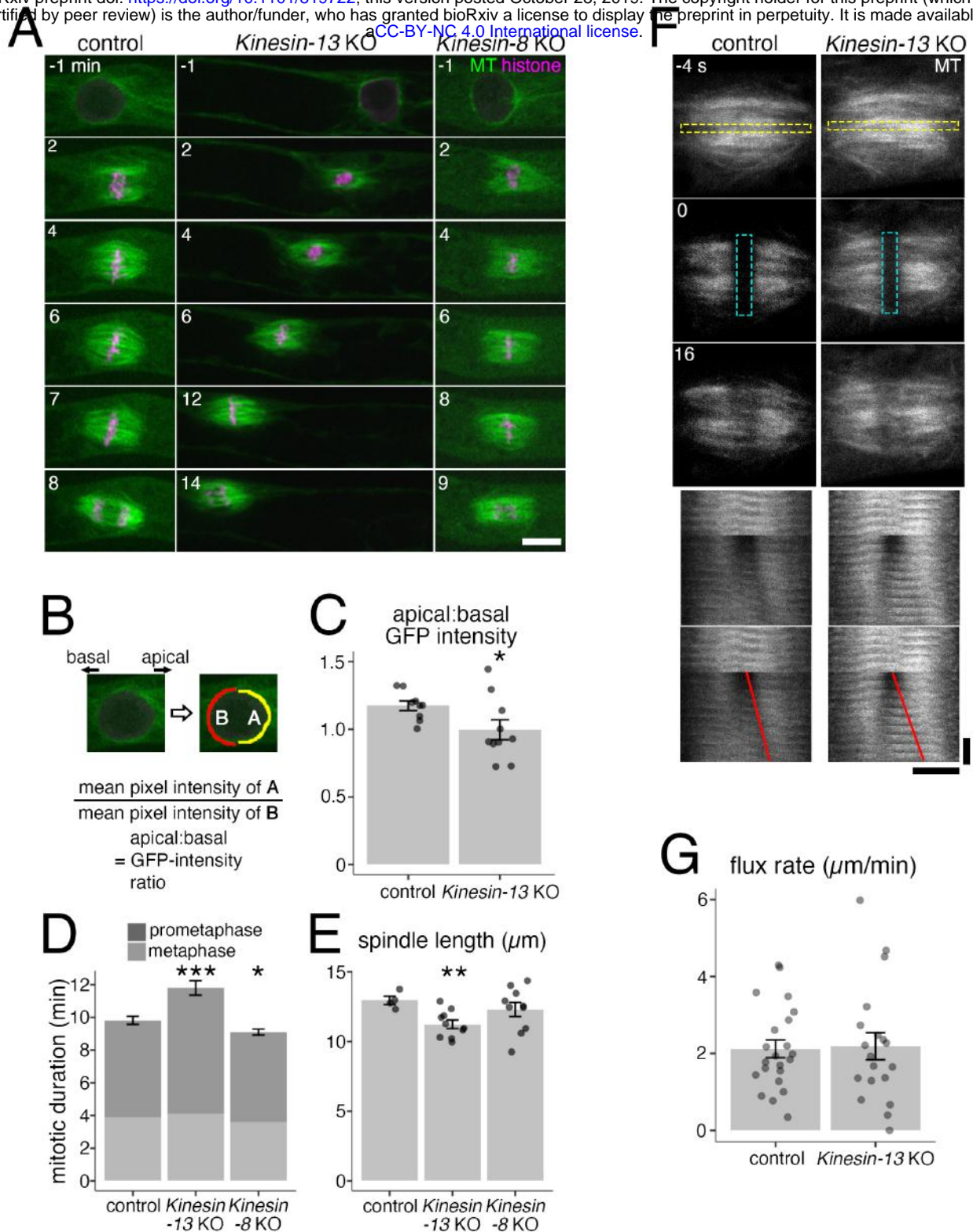
Figure 4

Figure 4: *Kinesin-13* KO moss shows defects in nuclear-proximal MT array, mitotic duration, and spindle length, but shows no difference in spindle flux rate.

(A) Mitosis of control (*GFP-tubulin/histoneH2B-mRFP*), *Kinesin-13* KO (GPH0438#6), and *Kinesin-8* KO (GPH0433#9) moss. *Kinesin-13* KO showed reduced metaphase spindle length, retrograde nuclear movement during prophase, increased mitotic duration, and loss of apical bias of nuclear-MTs. *Kinesin-8* KO did not show mitotic defects. Bar, 10 μm; NEBD, 0 min; left, basal side; right, apical side. **(B, C)** Apical:basal GFP-intensity ratio of GFP-tubulin around the nucleus 1 min before NEBD was measured as the ratio of GFP-tubulin intensities between apical and basal hemispheric circumference. Control (*GFP-tubulin/histoneH2B-mRFP*), 1.17 ± 0.04 (mean ± SEM; N=9; p-value < 0.05); *Kinesin-13* KO (GPH0438#6, 30), 1.00 ± 0.07 (mean ± SEM; N = 10). Points represent individual mitotic events. **(D)** Mitotic duration of control (*GFP-tubulin/histoneH2B-mRFP*), *Kinesin-13* KO (GPH0438#6, 30), and *Kinesin-8* KO (GPH0433#7, 9) moss as measured from NEBD to anaphase onset. Control, 9.8 ± 0.3 min (mean ± SEM; N = 11); *Kinesin-13* KO, 11.8 ± 0.4 min (mean ± SEM, N = 15; p-value < 0.001). *Kinesin-8* KO, 9.1 ± 0.2 min (mean ± SEM; N = 10; p-value < 0.05). The duration of prometaphase (from NEBD to chromosome alignment) and metaphase (chromosome alignment to anaphase onset) was also measured and shown. Data shown was pooled from two independent experiments. **(E)** Spindle length was measured at metaphase (defined as 1 min before anaphase onset) by obtaining the distance between midpoints of apical and basal spindle widths. Control (*GFP-tubulin/histoneH2B-mRFP*), 13.0 ± 0.3 μm (mean ± SEM; N = 4); *Kinesin-13* KO (GPH0438#30), 11.2 ± 0.3 μm (mean ± SEM; N = 10; p-value <0.01); *Kinesin-8* KO (GPH0433#9), 12.3 ± 0.5 μm (mean ± SEM; N = 10). Points represent individual mitotic events. **(F)** Spindle poleward flux of control (*GFP-tubulin/histoneH2B-mRFP*) and *Kinesin-13* KO (GPH0438#30) moss was examined in photobleaching experiments where GFP-tubulin signals on a strip along the metaphase plate was bleached. The bleached regions separating towards the poles are indicative of spindle poleward flux function. Horizontal bar, 5 μm; vertical bar; 12 s; yellow dashed rectangle in the top panel indicates region used to make time series (bottom panel); cyan dashed rectangle represents bleached region; red lines indicate the segmented lines drawn on the kymograph to obtain flux rate in (G). **(G)** Quantification of spindle poleward flux experiment as shown in (F). Control, 2.1 ± 0.2 μm/min (mean ± SEM; N = 22); *Kinesin-13* KO, 2.2 ± 0.4 μm/min (mean ± SEM; N = 19). Points represent individual mitotic events, shown are results from four independent experiments.
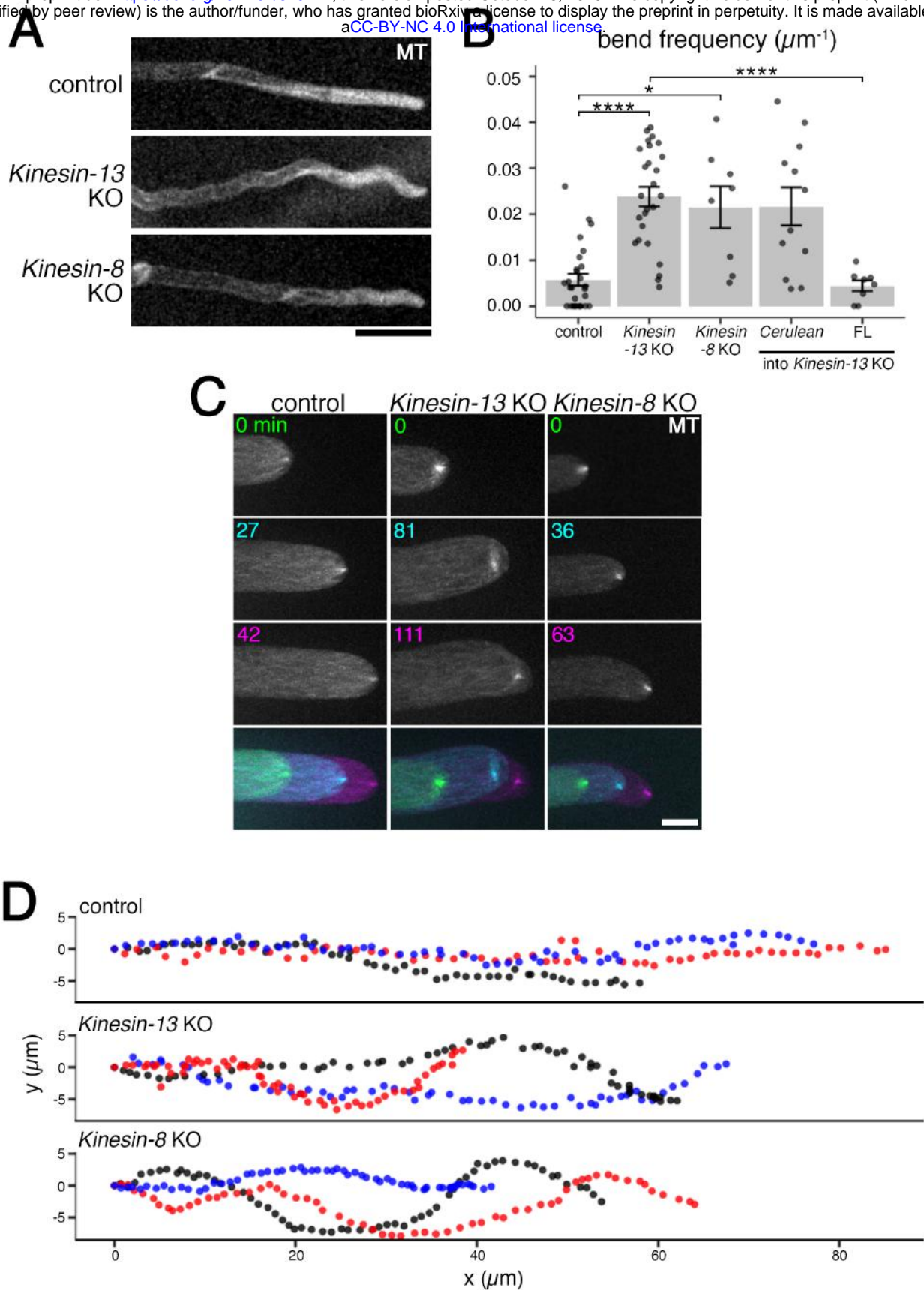
Figure 5

Figure 5: *Kinesin-13* and *-8* KO moss have wavy protonema filaments correlated with unstable MT foci positioning.

(A) Protonema filaments of control (*GFP-tubulin/histoneH2B-mRFP*), *Kinesin-13* KO (GPH0438#30), *Kinesin-8* KO (GPH0433#9) moss. Bar, 50 µm. **(B)** Waviness of protonema filaments measured as frequency of wavy bend (>18°) of protonema filaments over measured lengths. Control (*GFP-tubulin/histoneH2B-mRFP*), 0.006 ± 0.001 µm^{-1} (mean ± SEM; N = 28 filaments); *Kinesin-13* KO (GPH0438#30), 0.024 ± 0.002 µm^{-1} (mean ± SEM; N = 26 filaments; p-value < 0.0001); *Kinesin-8* KO (GPH0433#7), 0.022 ± 0.005 µm^{-1} (mean ± SEM; N = 8 filaments; p-value < 0.01); *Cerulean/Kinesin-13* KO (GPH0903#1), 0.022 ± 0.004 µm^{-1} (mean ± SEM; N = 12); *Kinesin-13b(full-length)-Cerulean/Kinesin-13* KO (GPH0899#10), 0.004 ± 0.001 µm^{-1} (mean ± SEM; N = 8; p-value < 0.0001). Points represent individual protonema filaments, results shown are from one experiment of at least four independent experiments. **(C)** MT foci at tip of caulonema cell of control (*GFP-tubulin/histoneH2B-mRFP*), *Kinesin-13* KO (GPH0438#30), *Kinesin-8* KO (GPH0433#9) moss. Images were acquired with z-sections at 0.3 µm intervals for 20 µm range, and maximum z-projections are displayed. Bottom panels show overlaid time series. Bar, 10 µm; colours in time series indicate different time points as labelled in top panels. **(D)** MT foci positions were tracked using FIJI MOSAIC plug-in 2D/3D particle tracker (Sbalzarini and Koumoutsakos, 2005) in time-lapse imaging data as in (C). (x, y) trajectories of three representative MT foci (shown in different colours) for each line are displayed. Each point represents subsequent positions at each time point, at 3 min intervals for 3 h. Same lines as in (B) are represented.
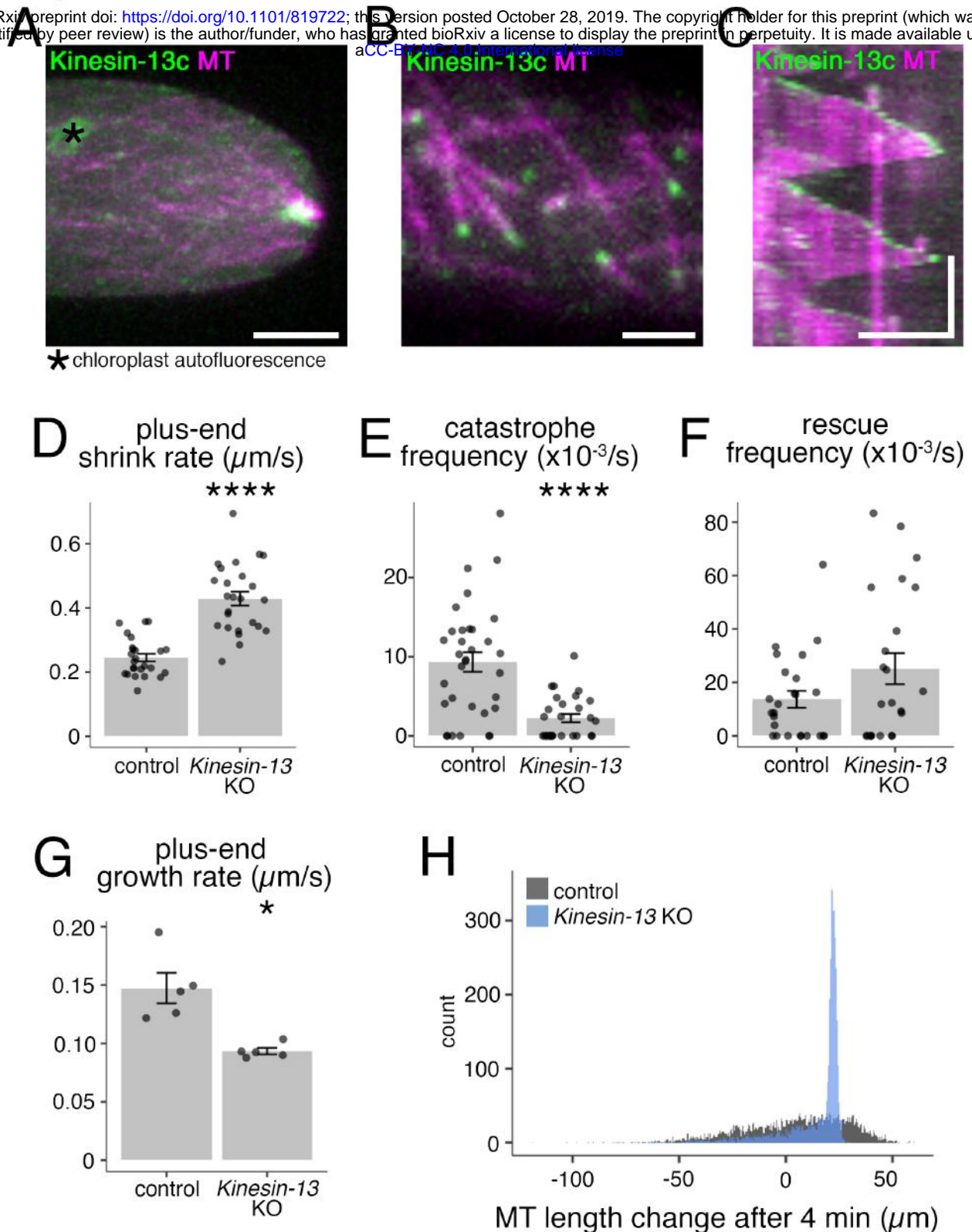
Figure 6

Figure 6: Kinesin-13 localises to the interphase MT network and depletion of Kinesin-13 results in increased shrink rate, reduced catastrophe frequency, increased rescue frequency, and reduced growth rate.

(A) MT foci of *Kinesin-13c-Citrine/mCherry-tubulin* (GPH0100#15) moss. Image was acquired at 0.3 µm intervals for 10 µm range; shown is maximum z-projection. Bar, 5 µm.
(B) Interphase MT network of *Kinesin-13c-Citrine/mCherry-tubulin* (GPH0100#15) moss. Images were acquired by oblique illumination fluorescence split-view microscopy to avoid chloroplast autofluorescence. Bar, 2 µm. **(C)** Kymograph of MT growth taken from imaging as in (B), taken every 3 s. Vertical bar, 2 min; horizontal bar, 5 µm. **(D)** Interphase MT plus-end shrink rate of control (*GFP-tubulin/histoneH2B-mRFP*, 0.245 ± 0.012 µm/s (mean ± SEM; N = 25 cells)) and *Kinesin-13* KO (GPH0438#30, 0.429 ± 0.021 µm/s (mean ± SEM; N = 25 cells; p-value < 0.0001)) moss. Points represent individual cells; results shown are from one experiment of two independent experiments. **(E)** Interphase MT catastrophe frequency of control (*GFP-tubulin/histoneH2B-mRFP*, 9.3 ± 1.2 x10⁻³/s (mean ± SEM; N = 33 cells)) and *Kinesin-13* KO (GPH0438#30, 2.2 ± 0.5 x10⁻³/s (mean ± SEM; N = 28 cells; p-value < 0.0001)). Points represent individual cells; results shown are from two independent experiments. **(F)** Interphase MT rescue frequency of control (*GFP-tubulin/histoneH2B-mRFP*, 14 ± 3 x10⁻³/s (mean ± SEM; N = 25 cells)) and *Kinesin-13* KO (GPH0438#30, 25 ± 6 x10⁻³/s (mean ± SEM; N = 23 cells)). Points represent individual cells; results shown are from two independent experiments. **(G)** Interphase MT plus-end growth rate of control (*EB1-Citrine/mCherry-tubulin*, GPH0379#2, 0.147 ± 0.013 µm/s (mean ± SEM; N = 5 cells, 50 MTs)) and *Kinesin-13* KO moss (GPH0577#11, 0.093 ± 0.003 µm/s (mean ± SEM; N = 5 cells, 50 MTs; p-value < 0.05)). Points represent individual cells. **(H)** Simulation of MT growth of 4,000 MTs in 4 min based on a probability model established using MT dynamics parameters from *in vivo* interphase MT dynamics analyses (D–G) (refer to Materials & Methods, and Table S4). Control MT dynamics parameters yielded approximately normal distributions of MT lengths and tended to have a larger population of MTs with longer lengths, with the longest 25% of MTs ranging between 23.4 to 59.8 µm in length. For MTs under *Kinesin-13* KO conditions, the distribution of MT length was narrower, with 50% of all MTs between 11.5 to 22.6 µm lengths, whereas the longest 25% of MTs ranged from 22.6 to 29.4 µm in length. Histogram bin width = 0.5 µm.
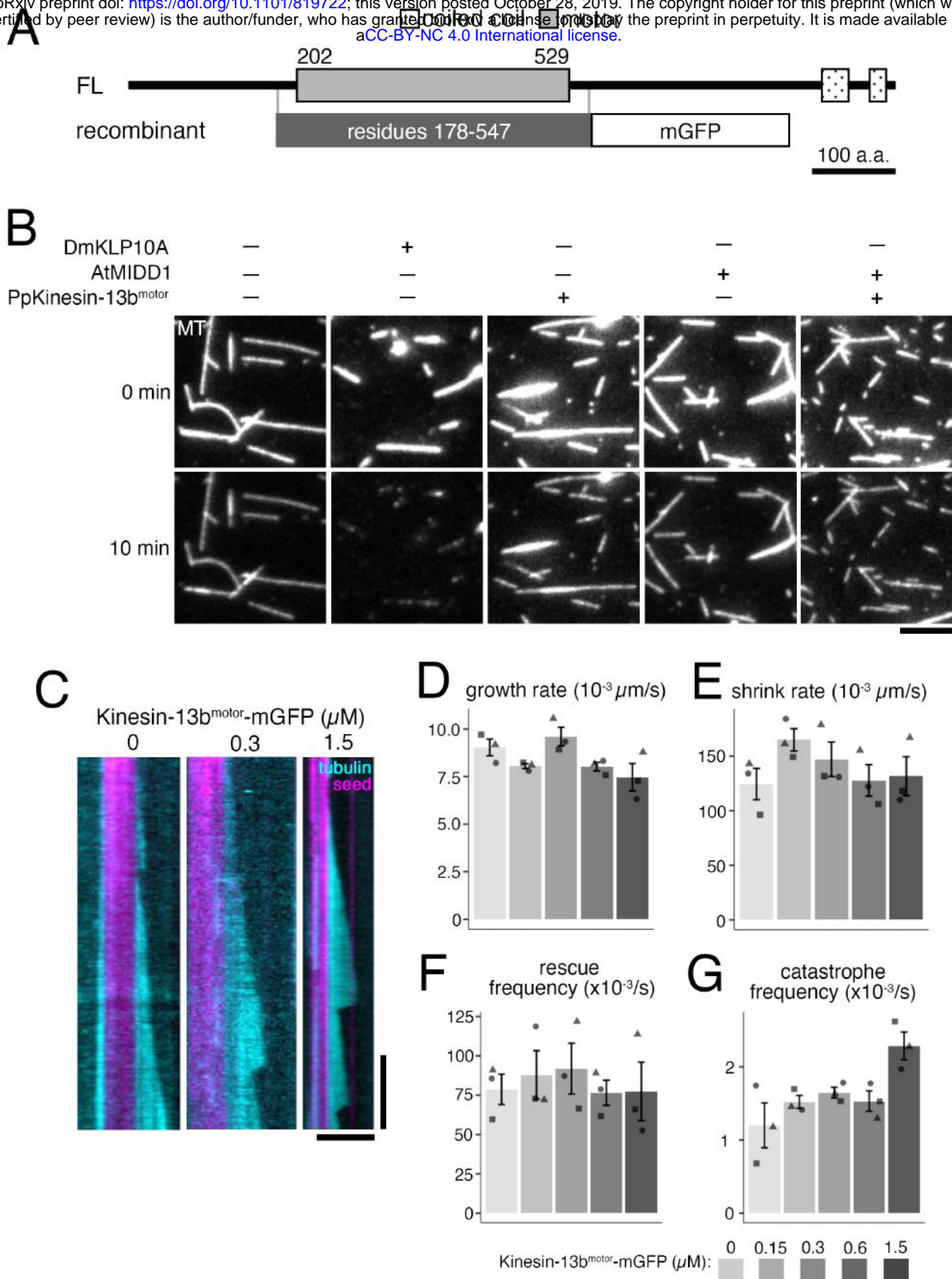
Figure 7

Figure 7: Recombinant Kinesin-13 does not depolymerise stabilised GMPCPP-MT seeds but shows MT catastrophe inducing activity.

(A) Protein domains of Kinesin-13b and recombinant Kinesin-13b^{motor}-mGFP construct. Protein domains were determined using InterPro. His-tag for affinity purification was attached to C-terminus of the recombinant protein. **(B)** *In vitro* MT depolymerisation assay using GMPCPP-stabilised MT seeds was performed using purified DmKLP10A, recombinant Kinesin-13b^{motor}-mGFP construct, AtMIDD1, AtMIDD1 and Kinesin-13b^{motor}-mGFP construct, and also under buffer only conditions. Only DmKLP10A successfully depolymerised MT seeds. The slight reduction in intensity in the bottom panels is due to photobleaching during imaging. All proteins were used at 200 nM except for AtMIDD1 which was at 100 nM. Bar, 5 μm. **(C)** Representative kymographs of *in vitro* MT dynamics polymerisation assays with Kinesin-13b^{motor}-mGFP construct at 0, 0.3, and 1.5 μM. Time-lapse imaging was performed with TIRF microscopy taken every 3 s. Brightness and contrast was manually adjusted. Vertical bar, 2 min; horizontal bar; 5 μm. **(D-G)** *In vitro* MT dynamics parameters were analysed from time-lapse imaging of *in vitro* MT dynamics polymerisation assays with Kinesin-13b^{motor}-mGFP construct at 0, 0.15, 0.3, 0.6, and 1.5 μM taken using TIRF microscopy at every 3 s. In particular, growth rate was observed to reduce slightly, from 9.0 ± 0.4 x10^{-3}μm/s (mean ± SEM; N = 3) in buffer only conditions, to 7.5 ± 0.7 x10^{-3}μm/s (mean ± SEM; N = 3) in 1.5 μM protein. Catastrophe frequency was observed to reproducibly increase with high concentrations of Kinesin-13b^{motor}-mGFP, having a catastrophe frequency of 2.3 ± 0.2 x10^{-3}/s (mean ± SEM; N = 3) at 1.5 μM protein, compared to 1.2 ± 0.3 x10^{-3}/s in buffer only conditions. Points represent mean values from independent experiments.
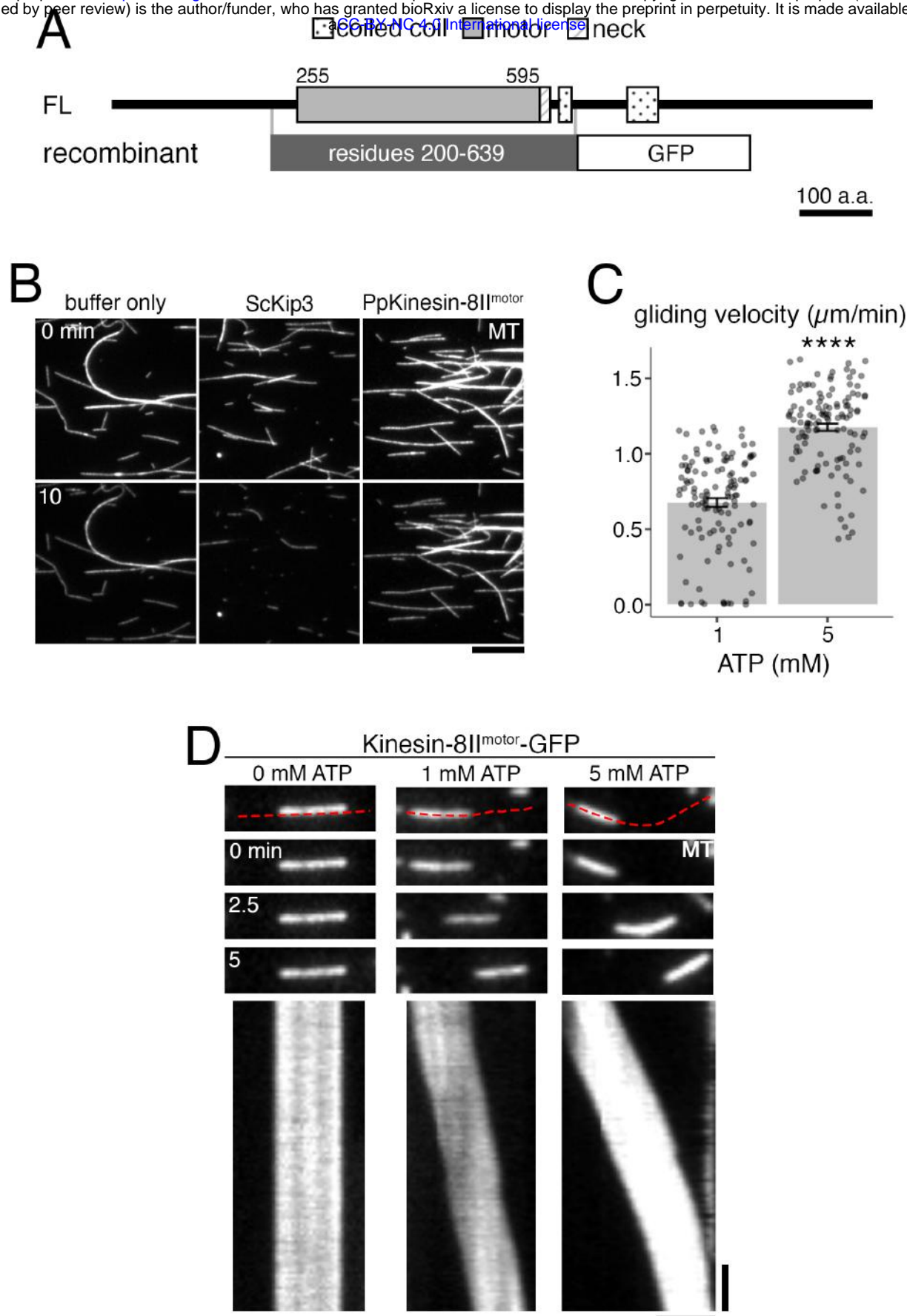
Figure 8

Figure 8: Recombinant Kinesin-8 motor does not depolymerise MTs but shows MT gliding activity.

(A) Protein domains of Kinesin-8II and recombinant Kinesin-8II[motor]-GFP construct. Protein domains were identified using InterPro. His-tag for affinity purification was attached to C-terminus of the recombinant protein. **(B)** *In vitro* MT depolymerisation assay using GMPCPP-stabilised MT seeds was performed using purified ScKip3, recombinant Kinesin-8II[motor]-GFP, and also under buffer only conditions. Only ScKip3 showed MT depolymerisation activity. The slight reduction in intensity in bottom panels is due to photobleaching during imaging. All proteins were used at 200 nM. Bar, 10 μm. **(C)** ATP-dependent MT gliding velocity of Kinesin-8II[motor]-GFP. 1 mM ATP, 0.68 ± 0.03 μm/min (mean ± SEM; N = 124 MTs); 5 mM ATP, 1.18 ± 0.02 μm/min (mean ± SEM; N = 121 MTs, p-value < 0.0001). **(D)** *In vitro* MT gliding assay using GMPCPP-stabilised MTs on Kinesin-8II[motor]-GFP which was immobilised on glass, at 0, 1, and 5 mM ATP. Red dotted line in top panel indicates segmented line used to draw kymographs (bottom panels). Gliding activity of Kinesin-8II[motor]-GFP was verified in 3 independent experiments. Vertical bar, 45 s; horizontal bar, 2 μm.

Parsed Citations

Collonnier, C., Epert, A, Mara, K., Maclot, F., Guyon-Debast, A, Charlot, F., White, C., Schaefer, D.G., and Nogue, F. (2017). CRISPR-Cas9-mediated efficient directed mutagenesis and RAD51-dependent and RAD51-independent gene targeting in the moss Physcomitrella patens. Plant Biotechnol J 15, 122-131.
Pubmed: Author and Title
Google Scholar: Author Only Title Only Author and Title

Cove, D. (2005). The moss Physcomitrella patens. Annu Rev Genet 39, 339-358.
Pubmed: Author and Title
Google Scholar: Author Only Title Only Author and Title

Deng, Z.Y., Liu, L.T., Li, T., Yan, S., Kuang, B.J., Huang, S.J., Yan, C.J., and Wang, T. (2015). OsKinesin-13A is an active microtubule depolymerase involved in glume length regulation via affecting cell elongation. Sci Rep 5, 9457.
Pubmed: Author and Title
Google Scholar: Author Only Title Only Author and Title

Desai, A, Verma, S., Mitchison, T.J., and Walczak, C.E. (1999). Kin I kinesins are microtubule-destabilizing enzymes. Cell 96, 69-78.
Pubmed: Author and Title
Google Scholar: Author Only Title Only Author and Title

Doonan, J.H., Cove, D.J., and Lloyd, C.W. (1985). Immunofluorescence microscopy of microtubules in intact cell lineages of the moss, Physcomitrella patens. I. Normal and CIPC-treated tip cells. J Cell Sci 75, 131-147.
Pubmed: Author and Title
Google Scholar: Author Only Title Only Author and Title

Doonan, J.H., Cove, D.J., and Lloyd, C.W. (1988). Microtubules and microfilaments in tip growth: evidence that microtubules impose polarity on protonemal growth in Physcomitrella patens. J Cell Sci 89, 533-540.
Pubmed: Author and Title
Google Scholar: Author Only Title Only Author and Title

Edzuka, T., and Goshima, G. (2019). Drosophila kinesin-8 stabilizes the kinetochore-microtubule interaction. J Cell Biol 218, 474-488.
Pubmed: Author and Title
Google Scholar: Author Only Title Only Author and Title

Eng, R.C., and Wasteneys, G.O. (2014). The microtubule plus-end tracking protein ARMADILLO-REPEAT KINESIN1 promotes microtubule catastrophe in Arabidopsis. Plant Cell 26, 3372-3386.
Pubmed: Author and Title
Google Scholar: Author Only Title Only Author and Title

Fujikura, U., Elsaesser, L., Breuninger, H., Sanchez-Rodriguez, C., Ivakov, A, Laux, T., Findlay, K., Persson, S., and Lenhard, M. (2014). At kinesin-13A modulates cell-wall synthesis and cell expansion in Arabidopsis thaliana via the THESEUS1 pathway. PLoS Genet 10, e1004627.
Pubmed: Author and Title
Google Scholar: Author Only Title Only Author and Title

Ganem, N.J., Upton, K., and Compton, D.A. (2005). Efficient mitosis in human cells lacking poleward microtubule flux. Curr Biol 15, 1827-1832.
Pubmed: Author and Title
Google Scholar: Author Only Title Only Author and Title

Gatt, M.K., Savoian, M.S., Riparbelli, M.G., Massarelli, C., Callaini, G., and Glover, D.M. (2005). Klp67A destabilises pre-anaphase microtubules but subsequently is required to stabilise the central spindle. J Cell Sci 118, 2671-2682.
Pubmed: Author and Title
Google Scholar: Author Only Title Only Author and Title

Gell, C., Bormuth, V., Brouhard, G.J., Cohen, D.N., Diez, S., Friel, C.T., Helenius, J., Nitzsche, B., Petzold, H., Ribbe, J., Schaffer, E., Stear, J.H., Trushko, A, Varga, V., Widlund, P.O., Zanic, M., and Howard, J. (2010). Microtubule dynamics reconstituted in vitro and imaged by single-molecule fluorescence microscopy. Methods Cell Biol 95, 221-245.
Pubmed: Author and Title
Google Scholar: Author Only Title Only Author and Title

Gicking, A.M., Swentowsky, K.W., Dawe, R.K., and Qiu, W. (2018). Functional diversification of the kinesin-14 family in land plants. FEBS Lett 592, 1918-1928.
Pubmed: Author and Title
Google Scholar: Author Only Title Only Author and Title

Goshima, G., and Vale, R.D. (2003). The roles of microtubule-based motor proteins in mitosis: comprehensive RNAi analysis in the Drosophila S2 cell line. J Cell Biol 162, 1003-1016.
Pubmed: Author and Title
Google Scholar: Author Only Title Only Author and Title

Goshima, G., and Scholey, J.M. (2010). Control of mitotic spindle length. Annu Rev Cell Dev Biol 26, 21-57.
Pubmed: Author and Title

Google Scholar: Author Only Title Only Author and Title

Gupta, M.L., Jr., Carvalho, P., Roof, D.M., and Pellman, D. (2006). Plus end-specific depolymerase activity of Kip3, a kinesin-8 protein, explains its role in positioning the yeast mitotic spindle. Nat Cell Biol 8, 913-923.
Pubmed: Author and Title
Google Scholar: Author Only Title Only Author and Title

Hertzer, K.M., Ems-McClung, S.C., Kline-Smith, S.L., Lipkin, T.G., Gilbert, S.P., and Walczak, C.E. (2006). Full-length dimeric MCAK is a more efficient microtubule depolymerase than minimal domain monomeric MCAK. Mol Biol Cell 17, 700-710.
Pubmed: Author and Title
Google Scholar: Author Only Title Only Author and Title

Hildebrandt, E.R., and Hoyt, M.A. (2000). Mitotic motors in Saccharomyces cerevisiae. Biochim Biophys Acta 1496, 99-116.
Pubmed: Author and Title
Google Scholar: Author Only Title Only Author and Title

Hirokawa, N., Noda, Y., Tanaka, Y., and Niwa, S. (2009). Kinesin superfamily motor proteins and intracellular transport. Nat Rev Mol Cell Biol 10, 682-696.
Pubmed: Author and Title
Google Scholar: Author Only Title Only Author and Title

Hiwatashi, Y., Sato, Y., and Doonan, J.H. (2014). Kinesins have a dual function in organizing microtubules during both tip growth and cytokinesis in Physcomitrella patens. Plant Cell 26, 1256-1266.
Pubmed: Author and Title
Google Scholar: Author Only Title Only Author and Title

Homma, N., Takei, Y., Tanaka, Y., Nakata, T., Terada, S., Kikkawa, M., Noda, Y., and Hirokawa, N. (2003). Kinesin superfamily protein 2A (KIF2A) functions in suppression of collateral branch extension. Cell 114, 229-239.
Pubmed: Author and Title
Google Scholar: Author Only Title Only Author and Title

Howard, J., and Hyman, A.A. (2007). Microtubule polymerases and depolymerases. Curr Opin Cell Biol 19, 31-35.
Pubmed: Author and Title
Google Scholar: Author Only Title Only Author and Title

Jonsson, E., Yamada, M., Vale, R.D., and Goshima, G. (2015). Clustering of a kinesin-14 motor enables processive retrograde microtubule-based transport in plants. Nat Plants 1.
Pubmed: Author and Title
Google Scholar: Author Only Title Only Author and Title

Kline-Smith, S.L., Khodjakov, A., Hergert, P., and Walczak, C.E. (2004). Depletion of centromeric MCAK leads to chromosome congression and segregation defects due to improper kinetochore attachments. Mol Biol Cell 15, 1146-1159.
Pubmed: Author and Title
Google Scholar: Author Only Title Only Author and Title

Kobayashi, T., Tsang, W.Y., Li, J., Lane, W., and Dynlacht, B.D. (2011). Centriolar kinesin Kif24 interacts with CP110 to remodel microtubules and regulate ciliogenesis. Cell 145, 914-925.
Pubmed: Author and Title
Google Scholar: Author Only Title Only Author and Title

Kofuji, R., and Hasebe, M. (2014). Eight types of stem cells in the life cycle of the moss Physcomitrella patens. Curr Opin Plant Biol 17, 13-21.
Pubmed: Author and Title
Google Scholar: Author Only Title Only Author and Title

Kosetsu, K., de Keijzer, J., Janson, M.E., and Goshima, G. (2013). MICROTUBULE-ASSOCIATED PROTEIN65 is essential for maintenance of phragmoplast bipolarity and formation of the cell plate in Physcomitrella patens. Plant Cell 25, 4479-4492.
Pubmed: Author and Title
Google Scholar: Author Only Title Only Author and Title

Kozgunova, E., and Goshima, G. (2019). A versatile microfluidic device for highly inclined thin illumination microscopy in the moss Physcomitrella patens. Sci Rep in press.
Pubmed: Author and Title
Google Scholar: Author Only Title Only Author and Title

Lee, T., Langford, K.J., Askham, J.M., Bruning-Richardson, A., and Morrison, E.E. (2008). MCAK associates with EB1. Oncogene 27, 2494-2500.
Pubmed: Author and Title
Google Scholar: Author Only Title Only Author and Title

Leong, S.Y., Yamada, M., Yanagisawa, N., and Goshima, G. (2018). SPIRAL2 Stabilises Endoplasmic Microtubule Minus Ends in the Moss Physcomitrella patens. Cell Struct Funct 43, 53-60.
Pubmed: Author and Title
Google Scholar: Author Only Title Only Author and Title

Li, W., Moriwaki, T., Tani, T., Watanabe, T., Kaibuchi, K., and Goshima, G. (2012). Reconstitution of dynamic microtubules with Drosophila XMAP215, EB1, and Sentin. J Cell Biol 199, 849-862.
Pubmed: Author and Title
Google Scholar: Author Only Title Only Author and Title

Lopez-Obando, M., Hoffmann, B., Gery, C., Guyon-Debast, A, Teoule, E., Rameau, C., Bonhomme, S., and Nogue, F. (2016). Simple and Efficient Targeting of Multiple Genes Through CRISPR-Cas9 in Physcomitrella patens. G3 (Bethesda) 6, 3647-3653.
Pubmed: Author and Title
Google Scholar: Author Only Title Only Author and Title

Lu, L., Lee, Y.R., Pan, R., Maloof, J.N., and Liu, B. (2005). An internal motor kinesin is associated with the Golgi apparatus and plays a role in trichome morphogenesis in Arabidopsis. Mol Biol Cell 16, 811-823.
Pubmed: Author and Title
Google Scholar: Author Only Title Only Author and Title

Maney, T., Wagenbach, M., and Wordeman, L. (2001). Molecular dissection of the microtubule depolymerizing activity of mitotic centromere-associated kinesin. J Biol Chem 276, 34753-34758.
Pubmed: Author and Title
Google Scholar: Author Only Title Only Author and Title

Mayr, M.I., Hummer, S., Bormann, J., Gruner, T., Adio, S., Woehlke, G., and Mayer, T.U. (2007). The human kinesin Kif18A is a motile microtubule depolymerase essential for chromosome congression. Curr Biol 17, 488-498.
Pubmed: Author and Title
Google Scholar: Author Only Title Only Author and Title

Menand, B., Calder, G., and Dolan, L. (2007). Both chloronemal and caulonemal cells expand by tip growth in the moss Physcomitrella patens. J Exp Bot 58, 1843-1849.
Pubmed: Author and Title
Google Scholar: Author Only Title Only Author and Title

Mennella, V., Rogers, G.C., Rogers, S.L., Buster, D.W., Vale, R.D., and Sharp, D.J. (2005). Functionally distinct kinesin-13 family members cooperate to regulate microtubule dynamics during interphase. Nat Cell Biol 7, 235-245.
Pubmed: Author and Title
Google Scholar: Author Only Title Only Author and Title

Menon, S., and Gupton, S.L. (2016). Building Blocks of Functioning Brain: Cytoskeletal Dynamics in Neuronal Development. Int Rev Cell Mol Biol 322, 183-245.
Pubmed: Author and Title
Google Scholar: Author Only Title Only Author and Title

Miki, H., Okada, Y., and Hirokawa, N. (2005). Analysis of the kinesin superfamily: insights into structure and function. Trends Cell Biol 15, 467-476.
Pubmed: Author and Title
Google Scholar: Author Only Title Only Author and Title

Miki, T., Nishina, M., and Goshima, G. (2015). RNAi screening identifies the armadillo repeat-containing kinesins responsible for microtubule-dependent nuclear positioning in Physcomitrella patens. Plant Cell Physiol 56, 737-749.
Pubmed: Author and Title
Google Scholar: Author Only Title Only Author and Title

Miki, T., Nakaoka, Y., and Goshima, G. (2016). Live cell microscopy-based RNAi screening in the moss Physcomitrella patens. Methods Mol Biol 1470, 225-246.
Pubmed: Author and Title
Google Scholar: Author Only Title Only Author and Title

Miki, T., Naito, H., Nishina, M., and Goshima, G. (2014). Endogenous localizome identifies 43 mitotic kinesins in a plant cell. Proc Natl Acad Sci U S A 111, E1053-1061.
Pubmed: Author and Title
Google Scholar: Author Only Title Only Author and Title

Moores, C.A, Yu, M., Guo, J., Beraud, C., Sakowicz, R., and Milligan, R.A. (2002). A mechanism for microtubule depolymerization by KinI kinesins. Mol Cell 9, 903-909.
Pubmed: Author and Title
Google Scholar: Author Only Title Only Author and Title

Moriwaki, T., and Goshima, G. (2016). Five factors can reconstitute all three phases of microtubule polymerization dynamics. J Cell Biol 215, 357-368.
Pubmed: Author and Title
Google Scholar: Author Only Title Only Author and Title

Nakaoka, Y., Kimura, A, Tani, T., and Goshima, G. (2015). Cytoplasmic nucleation and atypical branching nucleation generate endoplasmic microtubules in Physcomitrella patens. Plant Cell 27, 228-242.
Pubmed: Author and Title
Google Scholar: Author Only Title Only Author and Title

Nakaoka, Y., Miki, T., Fujioka, R., Uehara, R., Tomioka, A, Obuse, C., Kubo, M., Hiwatashi, Y., and Goshima, G. (2012). An inducible RNA interference system in Physcomitrella patens reveals a dominant role of augmin in phragmoplast microtubule generation. Plant Cell 24, 1478-1493.

Pubmed: Author and Title
Google Scholar: Author Only Title Only Author and Title

Nebenfuhr, A, and Dixit, R. (2018). Kinesins and Myosins: Molecular Motors that Coordinate Cellular Functions in Plants. Annu Rev Plant Biol 69, 329-361.

Pubmed: Author and Title
Google Scholar: Author Only Title Only Author and Title

Niwa, S., Nakajima, K., Miki, H., Minato, Y., Wang, D., and Hirokawa, N. (2012). KIF19A is a microtubule-depolymerizing kinesin for ciliary length control. Dev Cell 23, 1167-1175.

Pubmed: Author and Title
Google Scholar: Author Only Title Only Author and Title

Oda, Y., and Fukuda, H. (2013). Rho of plant GTPase signaling regulates the behavior of Arabidopsis kinesin-13A to establish secondary cell wall patterns. Plant Cell 25, 4439-4450.

Pubmed: Author and Title
Google Scholar: Author Only Title Only Author and Title

Ogawa, T., Saijo, S., Shimizu, N., Jiang, X., and Hirokawa, N. (2017). Mechanism of Catalytic Microtubule Depolymerization via KIF2-Tubulin Transitional Conformation. Cell Rep 20, 2626-2638.

Pubmed: Author and Title
Google Scholar: Author Only Title Only Author and Title

Ovechkina, Y., Wagenbach, M., and Wordeman, L. (2002). K-loop insertion restores microtubule depolymerizing activity of a "neckless" MCAK mutant. J Cell Biol 159, 557-562.

Pubmed: Author and Title
Google Scholar: Author Only Title Only Author and Title

Reddy, A.S., and Day, I.S. (2001). Kinesins in the Arabidopsis genome: a comparative analysis among eukaryotes. BMC Genomics 2, 2.

Pubmed: Author and Title
Google Scholar: Author Only Title Only Author and Title

Rogers, G.C., Rogers, S.L., and Sharp, D.J. (2005). Spindle microtubules in flux. J Cell Sci 118, 1105-1116.

Pubmed: Author and Title
Google Scholar: Author Only Title Only Author and Title

Rogers, G.C., Rogers, S.L., Schwimmer, T.A, Ems-McClung, S.C., Walczak, C.E., Vale, R.D., Scholey, J.M., and Sharp, D.J. (2004). Two mitotic kinesins cooperate to drive sister chromatid separation during anaphase. Nature 427, 364-370.

Pubmed: Author and Title
Google Scholar: Author Only Title Only Author and Title

Rounds, C.M., and Bezanilla, M. (2013). Growth mechanisms in tip-growing plant cells. Annu Rev Plant Biol 64, 243-265.

Pubmed: Author and Title
Google Scholar: Author Only Title Only Author and Title

Sabry, J.H., O'Connor, T.P., Evans, L., Toroian-Raymond, A, Kirschner, M., and Bentley, D. (1991). Microtubule behavior during guidance of pioneer neuron growth cones in situ. J Cell Biol 115, 381-395.

Pubmed: Author and Title
Google Scholar: Author Only Title Only Author and Title

Sbalzarini, I.F., and Koumoutsakos, P. (2005). Feature point tracking and trajectory analysis for video imaging in cell biology. J Struct Biol 151, 182-195.

Pubmed: Author and Title
Google Scholar: Author Only Title Only Author and Title

Schmidt, S., and Smertenko, A. (2019). Identification and characterization of the land-plant-specific microtubule nucleation factor MACET4. J Cell Sci 132.

Pubmed: Author and Title
Google Scholar: Author Only Title Only Author and Title

Shen, Z, Collatos, A.R., Bibeau, J.P., Furt, F., and Vidali, L. (2012). Phylogenetic analysis of the Kinesin superfamily from physcomitrella. Front Plant Sci 3, 230.

Pubmed: Author and Title
Google Scholar: Author Only Title Only Author and Title

Shipley, K., Hekmat-Nejad, M., Turner, J., Moores, C., Anderson, R., Milligan, R., Sakowicz, R., and Fletterick, R. (2004). Structure of a kinesin microtubule depolymerization machine. EMBO J 23, 1422-1432.

Pubmed: Author and Title
Google Scholar: Author Only Title Only Author and Title

Soppina, V., and Verhey, K.J. (2014). The family-specific K-loop influences the microtubule on-rate but not the superprocessivity of kinesin-3 motors. Mol Biol Cell 25, 2161-2170.

Pubmed: Author and Title
Google Scholar: Author Only Title Only Author and Title

Stumpff, J., von Dassow, G., Wagenbach, M., Asbury, C., and Wordeman, L. (2008). The kinesin-8 motor Kif18A suppresses kinetochore movements to control mitotic chromosome alignment. Dev Cell 14, 252-262.

Pubmed: Author and Title
Google Scholar: Author Only Title Only Author and Title

Stumpff, J., Wagenbach, M., Franck, A, Asbury, C.L., and Wordeman, L. (2012). Kif18A and chromokinesins confine centromere movements via microtubule growth suppression and spatial control of kinetochore tension. Dev Cell 22, 1017-1029.

Pubmed: Author and Title
Google Scholar: Author Only Title Only Author and Title

Tanaka, E., Ho, T., and Kirschner, M.W. (1995). The role of microtubule dynamics in growth cone motility and axonal growth. J Cell Biol 128, 139-155.

Pubmed: Author and Title
Google Scholar: Author Only Title Only Author and Title

Uehara, R., Tsukada, Y., Kamasaki, T., Poser, I., Yoda, K., Gerlich, D.W., and Goshima, G. (2013). Aurora B and Kif2A control microtubule length for assembly of a functional central spindle during anaphase. J Cell Biol 202, 623-636.

Pubmed: Author and Title
Google Scholar: Author Only Title Only Author and Title

Unsworth, A, Masuda, H., Dhut, S., and Toda, T. (2008). Fission yeast kinesin-8 Klp5 and Klp6 are interdependent for mitotic nuclear retention and required for proper microtubule dynamics. Mol Biol Cell 19, 5104-5115.

Pubmed: Author and Title
Google Scholar: Author Only Title Only Author and Title

Vidali, L., Augustine, R.C., Kleinman, K.P., and Bezanilla, M. (2007). Profilin is essential for tip growth in the moss Physcomitrella patens. Plant Cell 19, 3705-3722.

Pubmed: Author and Title
Google Scholar: Author Only Title Only Author and Title

Walczak, C.E., and Heald, R. (2008). Mechanisms of Mitotic Spindle Assembly and Function 265, 111-158.

Pubmed: Author and Title
Google Scholar: Author Only Title Only Author and Title

Walczak, C.E., Gayek, S., and Ohi, R. (2013). Microtubule-depolymerizing kinesins. Annu Rev Cell Dev Biol 29, 417-441.

Pubmed: Author and Title
Google Scholar: Author Only Title Only Author and Title

West, R.R., Malmstrom, T., Troxell, C.L., and McIntosh, J.R. (2001). Two related kinesins, klp5+ and klp6+, foster microtubule disassembly and are required for meiosis in fission yeast. Mol Biol Cell 12, 3919-3932.

Pubmed: Author and Title
Google Scholar: Author Only Title Only Author and Title

Wu, S.Z., and Bezanilla, M. (2018). Actin and microtubule cross talk mediates persistent polarized growth. J Cell Biol 217, 3531-3544.

Pubmed: Author and Title
Google Scholar: Author Only Title Only Author and Title

Yamada, M., and Goshima, G. (2018). The KCH Kinesin Drives Nuclear Transport and Cytoskeletal Coalescence to Promote Tip Cell Growth in Physcomitrella patens. Plant Cell 30, 1496-1510.

Pubmed: Author and Title
Google Scholar: Author Only Title Only Author and Title

Yamada, M., Miki, T., and Goshima, G. (2016). Imaging Mitosis in the Moss Physcomitrella patens. Methods Mol Biol 1413, 263-282.

Pubmed: Author and Title
Google Scholar: Author Only Title Only Author and Title

Yoshida, M.W., Yamada, M., and Goshima, G. (2019). Moss Kinesin-14 KCBP Accelerates Chromatid Motility in Anaphase. Cell Struct Funct 44, 95-104.

Pubmed: Author and Title
Google Scholar: Author Only Title Only Author and Title

Movie legends

Movie 1. Mitosis of control, Kinesin-13, and Kinesin-8 KO moss

GFP-tubulin and histoneH2B-mRFP were imaged with spinning disc confocal microscopy. NEBD, 0 min; Playback at 10 fps at 1 min intervals; left, basal side; right, apical side.

Movie 2. Spindle poleward flux of control and Kinesin-13 KO moss

GFP-tubulin on the mitotic spindle at metaphase was photobleached in a strip (0 min), and the migration of the photobleached strip towards the poles can be observed. Playback at 20 fps at 3 s intervals.

Movie 3. Protonema filament growth of control, Kinesin-13 and -8 KO moss.

GFP-tubulin was imaged with epifluorescence microscopy. Playback at 30 fps at 3 min intervals.

Movie 4. MT foci in protonema growth of control, Kinesin-13 and -8 KO moss

The MT foci was imaged with spinning disc confocal microscopy. Movies are maximum z-projections of z-stacks taken every 0.3 µm for a 20 µm range. Playback at 15 fps at 3 min intervals.

Movie 5. Localisation of Kinesin-13 during interphase

Kinesin-13c is shown representatively for the other two paralogues, which show similar localisation. Localisation at the MT foci (top panel) and the interphase endoplasmic MT array (bottom panel) were imaged with spinning disc confocal microscopy and oblique illumination fluorescence microscopy respectively. Playback at 15 fps at 3 s intervals.